Data Driven Fast Battery Health Diagnostics

Master of Science Thesis

Nandeesh Dharmalingam
Xiaoning Li

CHALMERS UNIVERSITY OF TECHNOLOGY
Gothenburg, Sweden 2024
www.chalmers.se

Master's thesis 2024

Data Driven Fast Battery Health Diagnostic

Leverage machine learning for battery health assessment

Nandeesh Dharmalingam
Xiaoning Li

CHALMERS
UNIVERSITY OF TECHNOLOGY

Department of Electrical Engineering
Division of Electric Power Engineering
Chalmers University of Technology
Gothenburg, Sweden 2024

Data Driven Fast Battery Health Diagnostic
Pioneering Data-Driven Solutions for Sustainable Vehicle Electrification
Nandeesh Dharmalingam
Xiaoning Li

Supervisor: Yizhou Zhang, Zeekr Technology Europe
Examiner: Torbjörn Thiringer, Department of Electrical Engineering

Master's Thesis 2024
Department of Electrical Engineering
Division of Electric Power Engineering
Chalmers University of Technology
SE-412 96 Gothenburg
Telephone +46 31 772 1000

Cover: Generated image representing advances in machine learning and AI, showing the future of battery diagnostics and the ease with which complex battery parameters can be obtained and used.

Typeset in LaTeX
Printed by Chalmers Reproservice
Gothenburg, Sweden 2024

Data Driven Fast Battery Health Diagnostics
NANDEESH DHARMALINGAM
XIAONING LI
Department of Electrical Engineering
Division of Electric Power Engineering
Chalmers University of Technology

Abstract

This thesis presents two semi-supervised deep learning diagnostic systems based on Gaussian Process Regression (GPR) combined with Multi-Layer Perceptron (MLP), Bidirectional Gated Recurrent Unit (BiGRU) and Autoencoder (AE). The primary objective is to assess battery health, which is a critical aspect of electric vehicles (EVs) and renewable energy systems. Traditional methods for evaluating battery health are often time-consuming, costly, and not suitable for immediate application. This study aims to overcome these challenges by adopting novel approaches.

To address these challenges, the research leverages recent developments in data analytics and machine learning to offer a scalable and effective approach for diagnosing battery health. A key achievement of this study is the use of semi-supervised learning techniques, which effectively utilize a small amount of labeled data together with a large amount of unlabeled data, significantly improving the accuracy of battery capacity estimates.

Through the analysis of extensive data from battery usage cycles, the research has developed quick, automated protocols that provide accurate, real-time monitoring of battery health. These systems enhance the management of battery usage in electric vehicles and renewable energy installations while supporting the broader adoption of sustainable energy practices.

The performance of both algorithms was evaluated using datasets from NASA and the Technical University of Munich (TUM). The experimental results demonstrate that the BiGRU+MLP+GPR algorithm achieves a Root Mean Square Error (RMSE) of 0.30 on the NASA dataset and 0.10 on the TUM dataset. In contrast, the AE+CNN+GPR algorithm yields RMSE values of 0.52 for the NASA dataset and 0.09 for the TUM dataset. Overall, the BiGRU+MLP+GPR algorithm exhibits greater robustness and stability. In addition to comparing the performance of these algorithms, this study provides a detailed analysis of their specific hyperparameter settings and investigates the impact of dataset availability on algorithm performance.

Keywords: State of Health (SoH), Electric Vehicles (EVs), Data-Driven Diagnostics, Machine Learning in Energy Storage, Battery Degradation Analysis, Semi supervised learning, Automated Diagnostic Protocols, Battery

Acknowledgements

We extend our deepest gratitude to our tutors, Yizhou Zhang and Torbjörn Thiringer, whose expert guidance and unwavering support were crucial throughout our academic journey. Their dedication to our progress was evident in their consistent availability for consultations and their willingness to share valuable insights that greatly enhanced our understanding and application of complex concepts. Their mentorship not only guided our research but also inspired us to strive for excellence in all aspects of our work.

Special thanks are due to Prof. Torbjörn Thiringer at Chalmers University, who served not only as our examiner but also as a significant mentor in our academic and professional development. His rigorous scholarly standards and constructive feedback were instrumental in refining our project, pushing us to integrate theoretical knowledge with practical applications. His encouragement during challenging phases of our research was invaluable in helping us maintain our focus and momentum.

Lastly, we wish to express our heartfelt gratitude to our families and friends. Their constant encouragement and unwavering support provided us with the strength and motivation needed to persevere through the challenges of this demanding academic endeavor. Their belief in our abilities and their emotional support were the bedrocks upon which we built our confidence and commitment. The success of this project is as much a testament to their love and belief in us as it is to our own efforts.

Nandeesh Dharmalingam and Xiaoning Li, Gothenburg, August 2024

Contents

1
Introduction

1.1 Background

Efficient battery health monitoring solutions are in high demand due to the growth of electric vehicles (EVs) and renewable energy systems. Batteries are critical components of these systems, providing energy storage for powering vehicles and storing renewable energy. However, over time, batteries degrade, reducing their capacity and performance, which can significantly affect the overall efficiency and reliability of EVs and renewable energy systems.

Assessing the State of Health (SoH) of a battery is a critical metric that indicates its current condition compared to its original state. Accurate and timely assessment of battery SoH is essential for optimizing battery usage, predicting remaining useful life, and ensuring safety and reliability in various applications. Data-driven approaches for battery health diagnostics are becoming increasingly popular due to the limitations of traditional methods, which can be time-consuming, costly, and impractical for real-time monitoring. These approaches offer a more efficient and effective solution to the challenges of battery health diagnosis. Utilizing data analytics and machine learning to analyze large-scale battery cycling data and develop fast and automated diagnostic methods.

A major goal and potential contribution of this work is the innovative use of semi supervised learning techniques, which leverage both limited labeled data and a larger volume of unlabeled data. This approach aims to markedly enhance the accuracy of battery capacity estimation.

1.2 Aim

The aim of this project is to develop a Data-Driven Fast Battery Health Diagnostic System capable of estimating the State of Health (SoH) of lithium-ion batteries, another main objective of this work would be using limited labeled data together with a large amount of unlabelled data to make a more accurate capacity estimation, which is one of the major goals and potential contributions. This will be achieved through the following objectives:

1. Develop an automatic data processing pipeline to analyze large-scale battery

cycling data efficiently and accurately.

2. Design and test rapid diagnostic protocols that enable quick battery health evaluations, potentially within minutes, using real-time data.

3. Develop machine learning algorithms capable of accurately estimating battery SoH based on the analyzed data.

In this study, we aim to design and explore two semi-supervised learning algorithms leveraging advanced neural network architectures and regression techniques. Specifically, the first algorithm is based on Bidirectional Gated Recurrent Units (BiGRU), Multilayer Perceptrons (MLP), and Gaussian Process Regression (GPR). The second algorithm integrates Convolutional Neural Networks (CNN), Autoencoders (AE), and Gaussian Process Regression (GPR).

1.3 Objective

The primary focus of this thesis is to address three key objectives outlined in Section 1.2. These objectives guide the investigation and are formulated into specific questions to be answered.

Dataset and algorithm performance

- How well the algorithm performs on different dataset?
- Can the extracted features effectively reflect the SoH status?
- How scalable is the algorithm to different datasets?

Algorithm hyperparameter optimization

- How do hyperparameters affect the performance of the algorithms?
- How to choose hyperparameters and backbone under different evaluation indicators?

Generalization to Unlabelled Datasets

How well does the developed method perform on unlabeled datasets where ground-truth SoH information is not available?

By answering these questions, this thesis aims to develop of a deep learning model that not only accurately predicts SoH based on existing data but also addresses the critical aspects of prediction speed and generalization to unlabelled datasets.

2

Theory

2.1 Lithium-ion Batteries

Lithium-ion batteries represent a state of art technology in the field of modern portable electronics and electric vehicles. These batteries are prized for their high energy density and rechargeability, which are enabled by the principle of lithium ions moving between the cathode and anode during charging and discharging cycles. Nevertheless, lithium-ion batteries present a number of safety concerns, particularly when subjected to overcharging, overheating, or physical damage, which may result in thermal runaway events. Furthermore, degradation mechanisms such as electrode particle fracturing, electrolyte decomposition, and capacity fade can compromise performance and longevity over time.

2.1.1 Components of a Lithium-ion Battery

- **Cathode:** Typically made from Lithium metal oxides, the cathode is the source of lithium ions and is crucial for the battery's voltage and capacity.
- **Anode:** Made from carbon materials like graphite, the anode stores lithium ions when the battery is charged.
- **Electrolyte:** A lithium salt solution in an organic solvent that facilitates the flow of lithium ions between the cathode and anode.
- **Separator:** A porous membrane that prevents physical contact between the cathode and anode avoiding short circuits while allowing ionic flow.

2.1.2 Basic Functionality

2.1.2.1 Charging process

During the charging process, a power source applies a voltage that is higher than the current voltage of the battery. This higher voltage is necessary to force lithium ions to move from the cathode (positive electrode) to the anode (negative electrode) through the electrolyte. As lithium ions migrate to the anode, they become embedded in the anode material, effectively storing energy within the battery. This

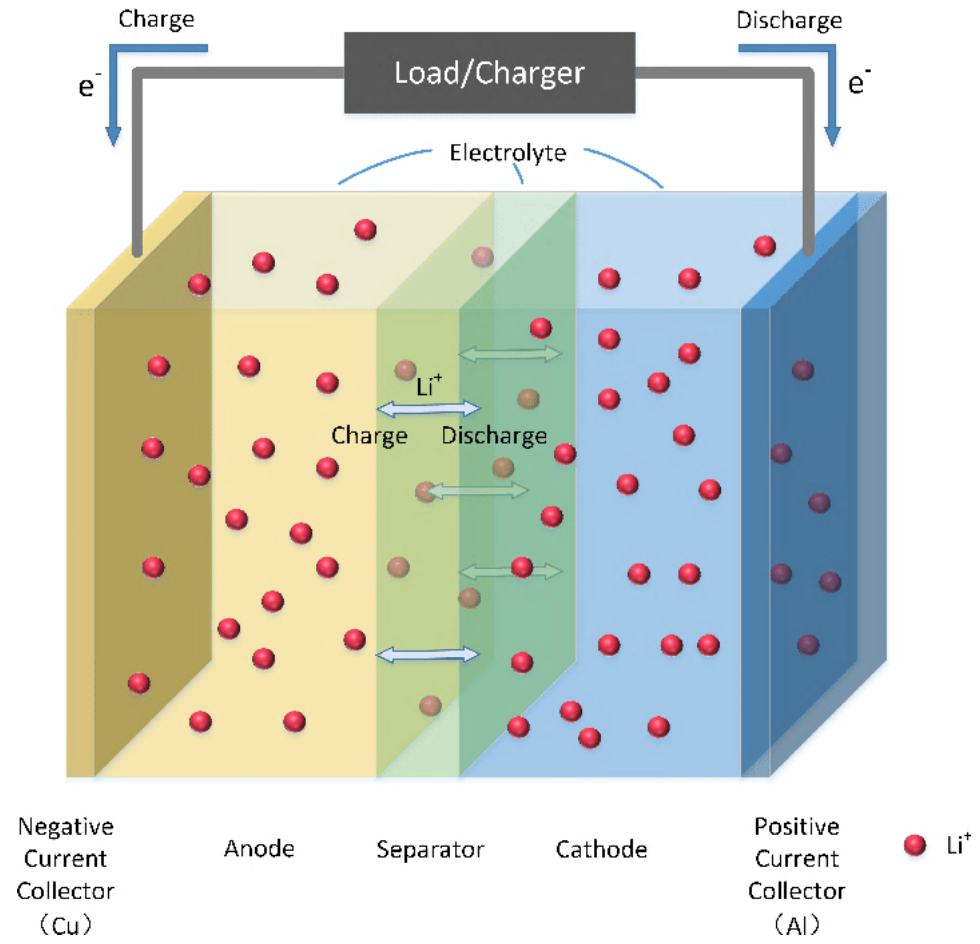

Figure 2.1: The overview of the working principle of the Li-ion battery [10].

movement of lithium ions and their storage in the anode is what allows the battery to hold and later deliver power when needed.

2.1.2.2 Discharging

When a device utilises the battery for power, the battery discharges. This process reverses the direction of ion movement, i.e., lithium ions flow from the anode back to the cathode, releasing stored energy. The electrons then travel through the external circuit to the device, generating an electric current that powers it.

2.1.3 Degradation factors

As outlined, the performance of Li-ion batteries is subject to deterioration over time, resulting from a combination of internal and external factors. Internal factors include changes in cell's mechanical and electrochemical properties, whereas external factors encompass operational conditions. Among the common aging mechanisms observed within batteries, the formation of the solid electrolyte interphase (SEI) and lithium plating have been identified as particularly detrimental, as evidenced by the findings of numerous researchers [11], [12].

- **Internal Resistance:** Internal resistance in a battery is defined as the opposition within the battery to the flow of electric current. As a battery ages, its internal resistance typically increases due to chemical and physical changes within the cell components.

  An increase in internal resistance results in elevated heat generation during the charging and discharging processes. This excess heat can accelerate the deterioration of the battery's materials. Furthermore, elevated internal resistance leads to diminished power delivery efficiency and a reduction in overall battery performance, since a greater proportion of energy is lost as heat rather than being utilized by the system [6][7].

- **Temperature:** The performance and lifespan of lithium-ion batteries are significantly influenced by temperature. Both high and low temperatures can have a adverse effect on the battery [7].

  - **High temperatures** can accelerate the degradation of battery materials, promote unwanted chemical reactions such as electrolyte decomposition, and increase the rate of SEI layer formation. This results in a loss of active material and a decrease in overall capacity.

  - **Low temperatures** can result in a reduction in the mobility of lithium ions in the electrolyte, which can lead to the formation of lithium plating on the anode during charging. Over time, this plating can cause a loss of capacity and an increase in the risk of internal short circuits.

- **Charge Rates (C-rates):** The charge rate, often expressed in terms of C-rate describes how fast a battery is charged and discharged relative to its maximum capacity. The rapid charging or discharging of a battery (high C-rates) can cause significant stress to the battery, resulting in the generation of excessive heat and rapid changes in voltage and current. This stress can aggravate degradation of the battery's components, particularly at the electrodes, and can lead to uneven distribution of lithium-ion, which can cause localised areas of overcharge or depletion. These conditions often result in a reduction in battery capacity and an accelerated battery lifespan [8].

- **Depth of Discharge (DoD):** It is a measure of the extent to which a battery is used in relation to its total capacity. It is expressed as a percentage of the battery capacity that has been discharged in relation to the overall capacity. Deeper discharges (higher DoD) put more strain on the battery because they require the battery to cycle through a greater range of its charge capacity. This increased cycling can lead to more rapid degradation of the battery's electrodes and electrolyte. Regularly discharging a battery to a low state of charge before recharging can lead to faster wear and tear, reducing the battery's lifespan and efficiency.

2.2 Degradation Mechanisms

The degradation of lithium-ion batteries is primarily driven by several key mechanisms, each contributing to the overall decline in battery performance. These mechanisms include the formation of the solid electrolyte interphase (SEI), lithium plating, and electrolyte decomposition. Each of these processes can affect the battery's ability to charge and discharge effectively, ultimately reducing its capacity and efficiency. This section provides a detailed examination of these degradation mechanisms and their implications for battery technology and health diagnostics.

- **Solid Electrolyte Interphase (SEI) Formation:** The SEI is a chemically stable layer that forms on the anode's surface during the initial charge cycles of a lithium-ion battery [14]. This layer results from the decomposition of electrolyte components when they first come into contact with the anode. The SEI acts as a barrier that consumes lithium ions, reducing the battery's efficiency and capacity over time. Elevated storage or cycling temperatures result in a higher diffusion rate, potentially leading to a more rapid growth of the SEI. Similarly, a higher current density can cause greater particle cracking, thereby contributing to the formation of a thicker SEI. In an Incremental capacity (IC) curve 2.5, SEI formation is indicated by a gradual decrease in peak heights related to lithium intercalation into the anode, as well as a shift in the voltage at which these peaks occur. This suggests a loss of active lithium and a change in the electrode surface properties [15] [16].

- **Lithium Plating:** Lithium plating occurs when metallic lithium forms on the surface of the anode instead of being inserted into the electrode material. This typically happens under conditions of high charge rates or low temperatures. Lithium plating is hazardous because it reduces cell capacity and poses a risk of short circuits. In the IC curve, lithium plating can be detected by the appearance of abnormal peaks at voltages lower than typical intercalation peaks, indicative of the formation of metallic lithium which does not contribute to normal battery operation.

- **Electrolyte Decomposition:** As the electrolyte breaks down, its ability to efficiently conduct lithium ions between the anode and cathode diminishes. This loss of ionic conductivity directly impacts the battery's ability to charge and discharge effectively, reducing its overall capacity. Electrolyte decomposition typically occurs under thermal stress or overcharge conditions, leading to the formation of gas and other byproducts that can cause swelling and reduce the efficiency of ionic transport across the electrolyte. In IC analysis, signs of electrolyte decomposition include the broadening of peaks and a shift in their positions, reflecting changes in the electrolyte's composition and a decrease in the overall ionic conductivity of the cell.

However, understanding the fundamental principles of lithium-ion battery technology is essential to recognize the significant role that materials play in determining the

performance and longevity of a battery. According to Tarascon and Armand (2001) [4], the selection of cathode and anode materials profoundly influences the efficiency and safety of a battery. The stability of the electrolyte across many charging cycles, especially under different temperature conditions, is crucial for maintaining the structural integrity of the battery.

Tarascon and Armand have also highlighted advancements in battery technology, including the exploration of new electrode materials that could potentially offer higher energy densities and improved safety features. These inputs are particularly relevant when considering the application of machine learning in battery health diagnostics. The degradation of battery materials, a key factor highlighted by Tarascon and Armand, can significantly influence the accuracy and effectiveness of machine learning models that predict the state of health (SoH) of batteries. By understanding these degradation mechanisms, machine learning models can be better designed to take these variables into account, enhancing their predictive accuracy.

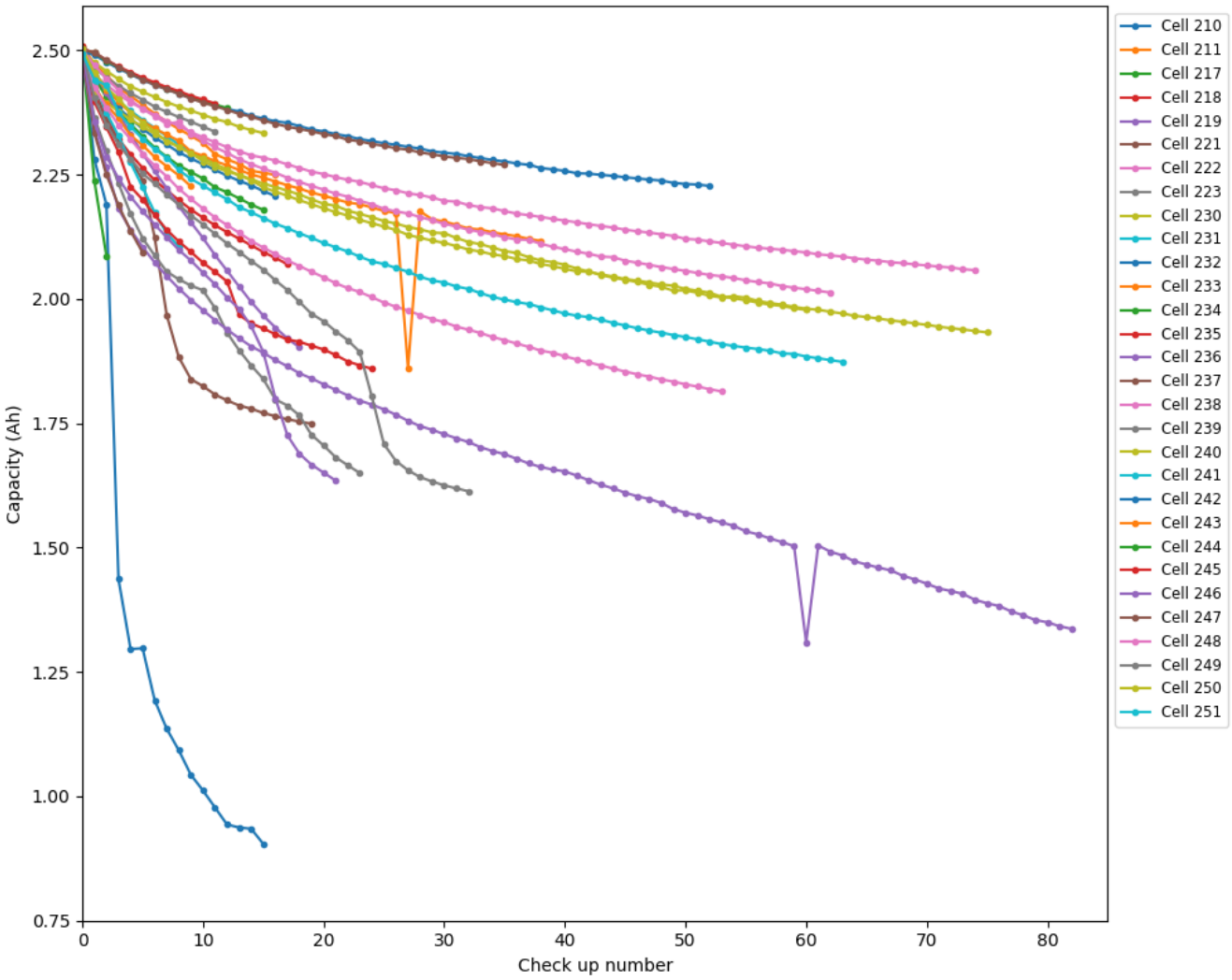

Figure 2.2: Capacity checkup of 30 cells from TUM dataset [3.1.2]

The results of a series of tests conducted on a number of cells are illustrated in figure 2.2. The cells were subjected to a number of different conditions, including depth of discharge (DOD), temperature, and current rates in while charging and discharging. The results show that the cells exhibited varying responses to these conditions and how they are degraded over time [3].

2.3 Relaxation of cell

In traditional battery health diagnostics, the state of health is primarily assessed by a method that involves full charge and discharge cycles followed by a relaxation period. This approach measures the battery's maximum capacity to indicate its health. After the cycling process, the batteries undergo a relaxation period that lasts several hours to a day, allowing all the transient chemical and physical processes to stabilize. The relaxation is critical because it enables voltage stabilization, ionic redistribution across the electrolyte and electrode interfaces, and a return to thermal equilibrium. These factors ensure that the measure taken post relaxation reflect the true health of the battery without the interference of operational stresses.

To address this advanced machine learning approaches propose a more efficient methodology by leveraging operational data collected during regular usage, thus the need for full cycle and prolonged relaxation periods can be eliminated. This method utilizes real-time data such as the voltage, current, and temperature, integrating machine learning algorithms to extract features and predict SoH from observable patterns. Features such as internal resistance, the phase changes which can be observed from the Incremental curves [3.3] like the peak height, the area under the curve are particularly insightful. These models trained on the data aim to correlate specific data patterns with battery health degradation, offering potential improvements in diagnostic precision and operational efficiency.

The shift from the traditional methodologies to a machine learning based approach represents a significant evolution in battery management, using real time, data driven that enhances predictive accuracy and reduce operational downtime. As such, this advanced diagnostic framework aligns closely with the contemporary demands of the automotive and energy storage industries, promising substantial benefits in terms of costs, efficiency, and battery life.

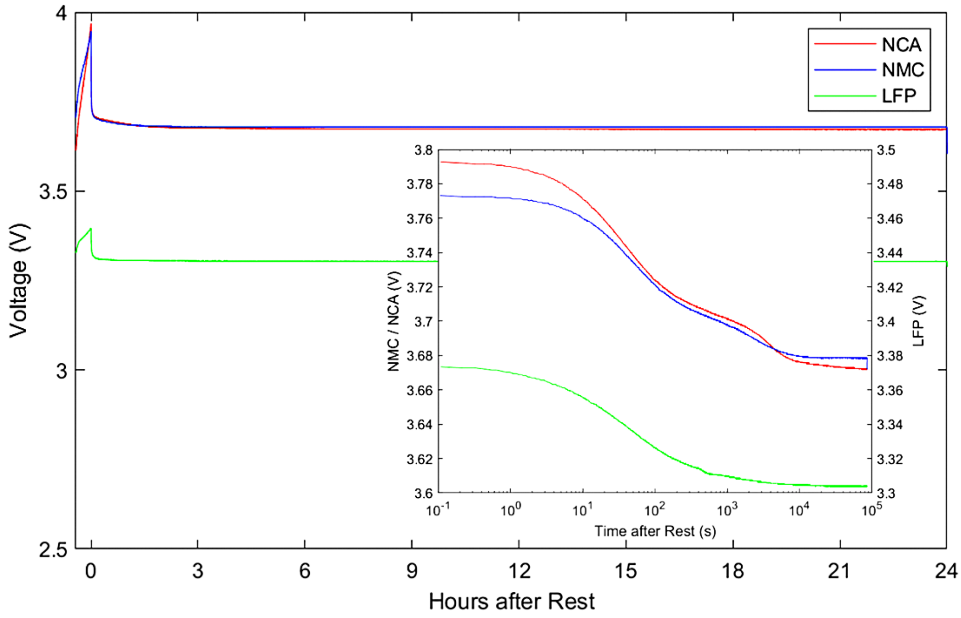

Figure 2.3: Twenty-four hour relaxation shown on a linear and logarithmic scale of NMC, NCA, and LFP chemistries.[5]

Figure 2.3 shows how the cell behaves while relaxing over the period which has been studied by Theuerkauf, D and Swan, L [5].

2.3.0.1 What happens during relaxation?

- **Voltage stabilization:** After charging or discharging, a battery's voltage can exhibit temporary spikes or dips. Allowing the battery to relax helps the voltage to stabilize at a more accurate equilibrium state, which is critical for precise voltage-based SoH measurements.

- **Diffusion Equilibrium:** Relaxation allows for the diffusion of ions to re-equilibrate across the electrolyte and electrode materials. This diffusion is crucial for maintaining the battery's capacity and internal resistance at stable levels, directly impacting the accuracy of capacity-based SoH assessments.

- **Thermal Equilibrium:**Batteries generate heat during operation, which can affect their performance and the reliability of diagnostic tests. Relaxation helps the battery return to a normal temperature, reducing the risk of thermal imbalances skewing SoH measurements.

- **Chemical Stability:** Some chemical reactions within the battery continue for a short time even after electrical activity stops. Relaxation allows these reactions to complete fully, ensuring that measurements reflect the true chemical state of the battery.

- **Accurate measurements:** For techniques like Electrochemical Impedance Spectroscopy (EIS), Incremental capacity analysis (ICA) which are used to

estimate SoH by measuring the internal resistance, having the battery in a stable, relaxed state is vital. This state ensures that the impedance measurements are not influenced by recent charging or discharging activities.

2.4 EVs capacity threshold

In electric vehicles, the SoH threshold is often set around **70% to 80%**. This means that once the battery's capacity to hold charge falls to 70-80% of its original capacity, it may no longer be suitable for continued use in the vehicle for the following reasons.

- **Range Reduction:** As the SoH decreases, so does the total energy storage capacity of the battery. This reduction in capacity means that the car can't go as far on a single charge as it could when the battery was new. If the range drops too much, it may not meet the practical needs of the user, making the car less effective for everyday use.

- **Performance Issues:** A lower SoH can lead to changes in the way the battery delivers power. The car may not accelerate as quickly or perform as well under certain conditions. This can affect the overall driving experience and could also affect safety in situations where rapid acceleration is required, such as when merging onto motorways.

- **Increased Charging Time and Frequency:** As the battery degrades, it may also take longer to charge and may need to be recharged more frequently, which can be inconvenient and time-consuming for users.

- **Safety concerns:** As batteries degrade, they can develop internal shorts due to the breakdown of battery materials or the accumulation of isolated lithium metal particles caused by plating. These shorts can cause localised overheating, further worsening degradation and increasing the risk of fire.

2.5 Incremental Capacity Analysis

Incremental Capacity (IC) analysis emerges as a critical diagnostic technique in the realm of battery health monitoring. This method involves measuring the differential capacity of the battery, which is the change in the charge capacity with respect to voltage, during charging cycle. By plotting the differential capacity against the cell voltage, IC curves are generated, which revel detailed characteristics about the battery's electrochemical reactions.

IC analysis is particularly adept at capturing the onset and progressing of degradation mechanisms. For instance, the formation of an SEI layer, lithium plating, and changes due to electrolyte decomposition all leads to specific alterations in the shape, position, and height of peaks in the IC curve. These alterations provide clues

about the type and severity of degradation occurring within the battery. Through careful analysis of these curves, explained further in chapter 3.2.2

In the following sections we have described briefly on how IC analysis is applied to detect these degradation signs, and how machine learning techniques can be utilized to automated the interpretation of IC data, thereby enhancing the precision and efficiency of battery diagnostics.

2.5.0.1 Objective for this analysis

- Identify significant peaks in the IC curves, which correspond to important electrochemical reactions within the battery.

- Calculate the Area under the curve (AUC) for each detected peak, providing a quantitative measure of the reaction's contribution to the overall battery behavior.

- Facilitate monitoring of battery degradation over time by tracking changes in peak characteristics and area under the curve values.

2.5.0.2 Electrochemical Reactions and Phase Transitions

- **The peaks** in the $\frac{dQ}{dV}$ vs voltage plot correspond to specific electrochemical reactions and phase transitions within the battery materials. In lithium-ion batteries, these transitions are often associated with the intercalation and de-intercalation processes of lithium ions in the anode and cathode materials.

- **Voltage Range** 3.4V to 3.8V is significant for many lithium-ion batteries, particularly those using lithium nickel manganese cobalt oxide (NMC) cathode and graphite anode. During charging, lithium ions are intercalated into the graphite anode, and this process can exhibit distinct peaks at certain voltages where phase transitions occur.

2.5.0.3 Cathode Material Transitions

- In NMC batteries, the cathode undergoes multiple phase transitions as lithium ions are extracted during charging. These transitions manifest as peaks in the IC curve. For example, an NMC cathode can exhibit multiple redox reactions involving nickel, manganese, and cobalt, each contributing to specific peaks in the IC plot 3.2.2.

- The voltage range of 3.4V to 3.8V often includes transitions related to the nickel redox reactions in NMC materials. These reactions are responsible for significant changes in capacity with small changes in voltage, hence the observed peaks.

2.5.0.4 Anode Material Contributions

- The graphite anode also contributes to the IC peaks. During lithium intercalation, graphite undergoes staging transitions, where lithium atoms occupy specific sites within the graphite structure. These staging transitions can create distinct peaks in the IC curve.

- Typical staging transitions for graphite occur around the voltages you observed, with notable stages at approximately 3.6V, reflecting the formation of different lithium-graphite phases.

2.5.0.5 Solid Electrolyte Interphase (SEI) Formation

The SEI layer forms on the anode surface during initial charging cycles and continues to evolve, impacting the IC curve. The formation and growth of the SEI can create additional peaks or modify existing ones in the voltage range you observed.

2.6 Machine Learning

Machine learning is a branch of artificial intelligence that focuses on developing algorithms and statistical models that enable computers to learn from and make predictions or decisions based on data. It encompasses a variety of techniques such as supervised learning, unsupervised learning, and reinforcement learning [21].

Deep learning is a subset of machine learning that focuses on algorithms inspired by the structure and function of the brain, known as artificial neural networks. Specifically, deep learning refers to neural networks with multiple layers, hence the term "deep". These layers enable the model to learn and represent data with increasing levels of abstraction [21].

Currently, there are various specialized methods for predicting battery capacity using machine learning. Traditional data-driven approaches include predictions using Support Vector Machines (SVM) [22] and methods employing Gaussian Process Particle Filters (GPPF) [23]. Additionally, Gaussian Process Regression (GPR) [24] has also seen widespread application.

However, with the decreasing cost of computational power and advancements in artificial intelligence algorithms, deep learning methods have gained extensive usage. For instance, CNN-RNN [25] algorithms and improved recurrent neural network (RNN) architectures such as Long Short-Term Memory (LSTM) [26] are now commonly used for prediction tasks. Furthermore, examples of transfer learning across different battery datasets have emerged.

Overall, mature prediction methods typically rely on large annotated datasets, which are somewhat limited for real-time diagnostics of practical batteries that require rapid assessment. Based on the current situation as well as the requirements, we produced two semi-supervised deep learning models for predicting battery capacity using partially labelled datasets based on a combination of deep learning architectures

2.7 The sub-algorithm

The two algorithms in this study are built from multi-seeded algorithms, this section will introduce the sub-frameworks used in both algorithms and their underlying principles.

2.7.1 Gaussian Process Regression (GPR)

Gaussian Process Regression (GPR) is a powerful non-parametric Bayesian approach used for regression tasks. It models the relationship between input variables $\mathbf{x}$ and output variables $\mathbf{y}$ as a joint Gaussian distribution 3.2.4.

$$\begin{bmatrix} \mathbf{y} \\ \mathbf{y}_* \end{bmatrix} \sim \mathcal{N}\left(\begin{bmatrix} \mu \\ \mu_* \end{bmatrix}, \begin{bmatrix} K(\mathbf{X},\mathbf{X}) + \sigma_n^2 I & K(\mathbf{X},\mathbf{X}_*) \\ K(\mathbf{X}_*,\mathbf{X}) & K(\mathbf{X}_*,\mathbf{X}_*) \end{bmatrix} \right),$$

- $\mathbf{y}$ and $\mathbf{y}_*$ are vectors of observed and unobserved target values, respectively.
- μ and μ_* are mean vectors.
- $K(\cdot,\cdot)$ represents a covariance function (kernel) that captures the similarity between pairs of input data points.
- σ_n^2 denotes the noise variance.
- $\mathbf{X}$ and $\mathbf{X}_*$ are matrices of input variables corresponding to observed and unobserved data points.

GPR computes a posterior distribution of functions by Bayesian inference, allowing predictions and estimation of uncertainty at new input points $\mathbf{X}_*$.

2.7.2 Types of Gaussian Kernels

In the algorithm used later we used three different Gaussian kernels, The following is a detailed introduction to the three Gaussian kernels.

2.7.2.1 Radial Basis Function (RBF) kernel

The Radial Basis Function (RBF) kernel is commonly used in GPR to define the covariance matrix $K(\mathbf{X},\mathbf{X})$

$$k_{\text{RBF}}(x_i, x_j) = \exp\left(-\frac{\|x_i - x_j\|^2}{2l^2}\right) \tag{2.1}$$

where x_i and x_j are two input data points, $\|x_i - x_j\|$ denotes the Euclidean distance between them, and l is the length-scale parameter that controls the width of the kernel. The Gaussian kernel is infinitely differentiable, making it suitable for modeling very smooth functions.

2.7.2.2 Matérn Kernel

The Matérn kernel introduces a parameter ν that controls the smoothness of the resulting function

$$k_{\text{Matérn}}(r) = \frac{2^{1-\nu}}{\Gamma(\nu)}\left(\frac{\sqrt{2\nu}r}{l}\right)^{\nu} K_\nu\left(\frac{\sqrt{2\nu}r}{l}\right) \tag{2.2}$$

where $r = \|x_i - x_j\|$, l is the length-scale parameter, ν is the smoothness parameter, $\Gamma(\nu)$ is the Gamma function, and K_ν is the modified Bessel function of the second kind. The Matérn kernel can take simpler forms for specific values of ν, such as $\nu = 0.5$, $\nu = 1.5$, and $\nu = 2.5$, corresponding to different levels of differentiability.

2.7.2.3 Rational Quadratic (RQ) Kernel

The Rational Quadratic kernel can be seen as a scale mixture of Gaussian kernels with different length-scales. It is defined as

$$k_{\text{RQ}}(x_i, x_j) = \left(1 + \frac{\|x_i - x_j\|^2}{2\alpha l^2}\right)^{-\alpha}, \tag{2.3}$$

where $\|x_i - x_j\|$ is the Euclidean distance between x_i and x_j, l is the length-scale parameter, and α is the shapeparameter. The RQ kernel interpolates between the Gaussian kernel (when $\alpha \to \infty$) and the polynomial kernel (for finite α).

In summary, the choice of Gaussian process regression (GPR) kernel depends largely on the desired smoothness and flexibility characteristics for modeling data.The specific comparison of the three Gaussian kernel structures is in section 5.2.2 Gaussian Process Regression with these kernels has found applications in various domains. Since it can predict the trend of required data based on partial data, it is very suitable for application in partially labeled tram datasets.

2.7.3 Convolutional Neural Networks (CNNs)

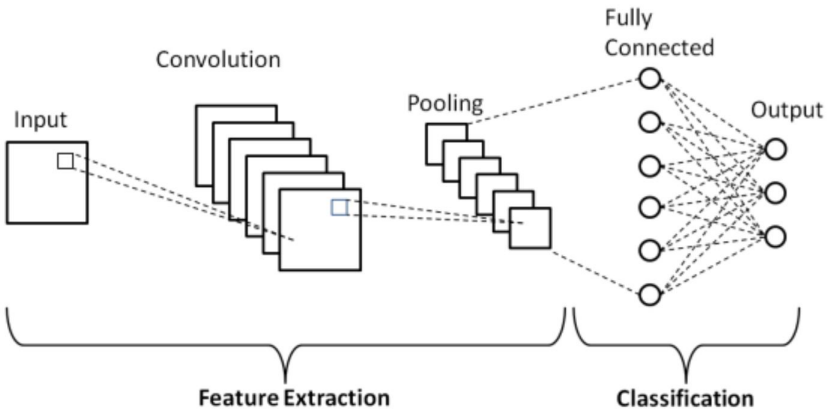

Figure 2.4: Basic CNN Schematic [17].

Convolutional Neural Networks (CNNs) are a class of deep neural networks designed to process structured grid-like data, such as images. Its structure diagram is shown in figure 2.4. CNN has four main structures:

- **Convolutional Layers:** These layers apply convolution operations to input data using learnable filters (kernels). The convolution operation involves sliding the filters over the input data to extract local patterns and features.

- **Pooling Layers:** Pooling layers downsample the spatial dimensions of the feature maps generated by convolutional layers. This helps reduce computational complexity and control overfitting.

- **Activation Functions:** Typically, activation functions like ReLU (Rectified Linear Unit) are applied after convolutional and pooling operations to introduce non-linearity into the network.

- **Fully Connected Layers:** These layers connect every neuron in one layer to every neuron in the next layer, enabling the network to learn global patterns and make predictions.

Convolutional Neural Networks (CNNs) utilize parameter sharing and spatial hierarchy to automatically learn and extract features from data, making them highly suitable for tasks related to image processing. Battery datasets, despite being different in nature from images, often exhibit similar structural characteristics that make CNNs effective for feature extraction.

2.7.4 Bidirectional Gated Recurrent Unit (BiGRU)

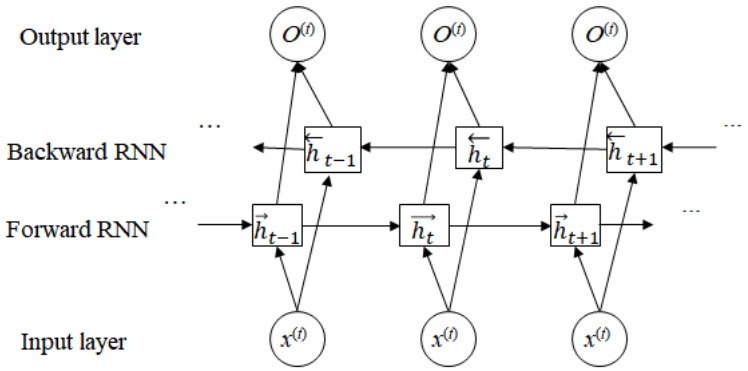

Figure 2.5: Basic BiGRU Schematic [19].

Bidirectional Gated Recurrent Unit (BiGRU) is a variant of recurrent neural networks (RNNs) that combines the concepts of bidirectional processing and gated mechanisms for improved sequence modeling. Its structure diagram is shown in figure 2.5

There are three Components of BiGRU

- **Gated Recurrent Unit (GRU):** GRU is a type of RNN that includes gating mechanisms to control the flow of information through the network. It consists of reset and update gates, which regulate the flow of information and decide what to update and forget.

- **Bidirectional Processing:** BiGRU processes input sequences in two directions: forward and backward. This allows the model to capture dependencies from both past and future contexts, enabling better understanding of sequential data.

- **Concatenation of Outputs:** Outputs from both directions are concatenated at each time step, providing a more comprehensive representation of the input sequence for subsequent layers or tasks.

BiGRU is particularly effective in tasks like natural language processing (NLP) due to its ability to capture dependencies in sequential data. Similarly, battery data, which is also time-series data, exhibits strong temporal dependencies akin to those found in NLP tasks. Therefore, BiGRU models can perform well in predicting battery-related variables by effectively capturing the temporal relationships within the data.

2.7.5 The Multilayer Perceptron (MLP)

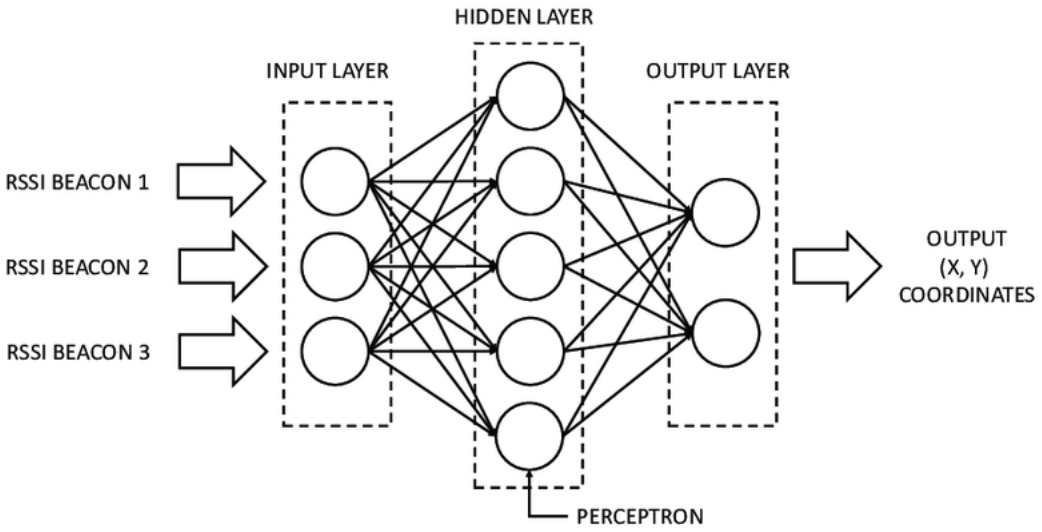

Figure 2.6: Basic MLP Schematic [18].

The Multilayer Perceptron (MLP) is a classic feedforward neural network architecture widely used for supervised learning tasks, such as classification and regression. It consists of multiple layers of nodes (neurons), its structure diagram is shown in 2.6 and itsorganized in a hierarchical manner:

- **Input Layer:** The first layer receives input features from the dataset.
- **Hidden Layers:** Intermediate layers between the input and output layers. Each hidden layer typically applies an activation function to its inputs and passes the result to the next layer.
- **Output Layer:** The final layer produces the network's predictions or outputs based on the activations from the preceding layers.

MLP excels at predicting hierarchical patterns in data, allowing them to effectively map raw battery datasets onto features relevant to battery capacity.

2.7.6 Autoencoder Algorithm(AE)

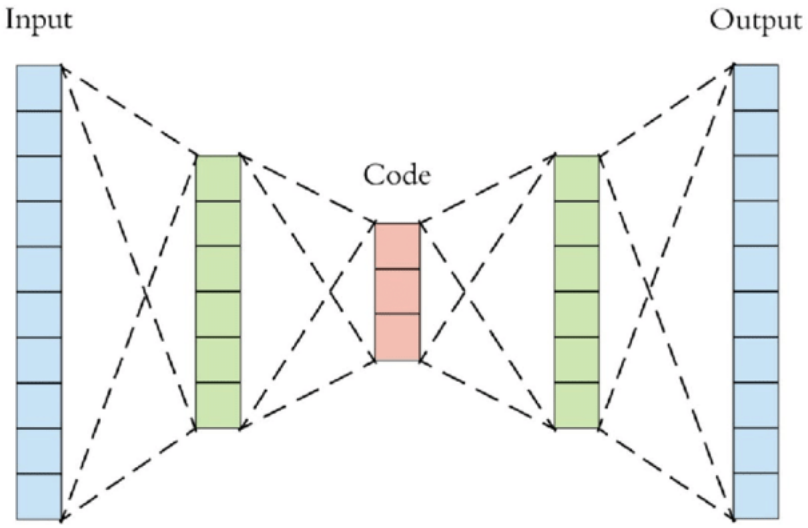

Figure 2.7: Autoencoder Structure [20].

The Autoencoder algorithm is a type of artificial neural network used for learning efficient representations of data, typically for dimension reduction, feature learning, or data compression. It consists of two main components: an encoder and a decoder. Here's a brief overview of how it works.its structure diagram is shown in figure 2.7. Its basic principle as follow:

1. **Encoder (Mapping Function):**
   The encoder function $h = f(x)$ maps the input data x to a hidden representation h. This can be represented as a neural network layer where h is a compressed representation of x.

2. **Decoder (Reconstruction Function):**
   The decoder function $r = g(h)$ reconstructs the input data x from the hidden representation h. The goal is to make output r as close to x as possible.

3. **Objective:**
   The autoencoder aims to minimize the reconstruction error between the input x and the output r. Commonly, the Mean Squared Error (MSE) is used as the loss function.
   $$\mathcal{L}(x, r) = ||x - r||^2$$
   Training the autoencoder involves adjusting the weights of the neural network to minimize this reconstruction error across a dataset.

Since the autoencoder can extract features without any labeled dataset, it is very suitable for the daily use of battery datasets.

2.8 Algorithm Implementation

Most battery capacity prediction methods rely on fully annotated standard battery datasets. Algorithms based on such datasets often struggle to be applied to dynamic real-world datasets. Furthermore, predicting battery capacity directly from raw battery data is a challenge in dynamic environments. Therefore, extracting effective features from raw battery datasets before predicting battery capacity can lead to broader and more practical application scenarios. Based on the above requirements two data-driven deep learning battery capacity prediction methods is obtained by combining the basic algorithms.

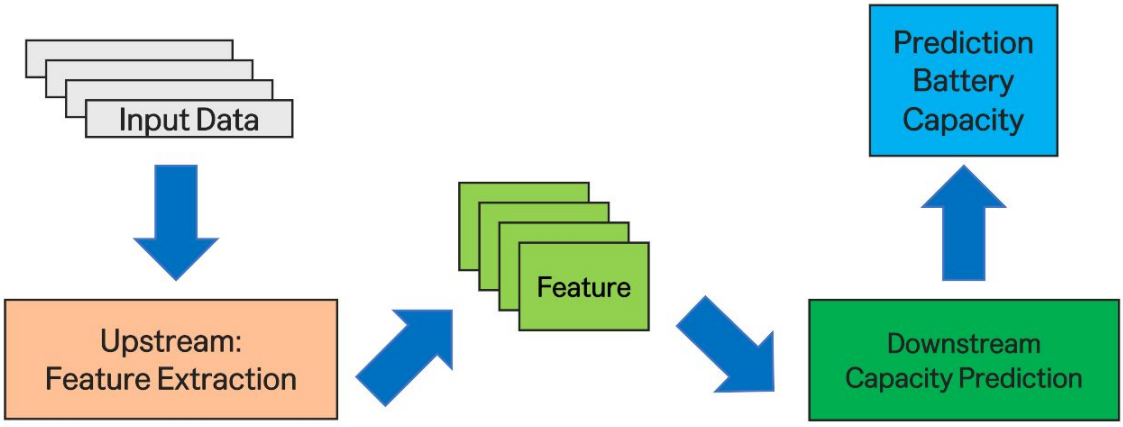

Figure 2.8: Overall structure of the algorithm

The overall idea is a large two-step scheme based on combining upstream and downstream. The upstream learns from the original dataset to obtain effective battery features, after which semi-supervised learning is carried out with a small amount of labelled battery capacity data from the downstream as well as the extracted features from the upstream, thus obtaining a model that can predict battery capacity. The flow chart is shown in figure 2.8

The first algorithm is based on BiGRU, MLP, and GPR techniques. Due to the excellent performance of BiGRU in extracting features from long time-series data, it was chosen as the algorithm for extracting original time features of battery data. After extracting the time features, an MLP algorithm was employed to map these features to the four annotated capacity features can be seen in figure 3.1. Finally, to enable prediction using partially labeled data, a semi-supervised GPR algorithm was selected as the downstream model. This algorithm uses the input capacity features to predict the true capacity of the battery. The specific implementation steps of both algorithms are detailed in section 4.1

To further reduce the reliance on labeled datasets and simulate real-world battery datasets, self-supervised learning was employed with an autoencoder as the feature extraction upstream algorithm for our second approach. After feature extraction via the autoencoder, the obtained capacity features are fed into the downstream GPR model for capacity prediction. The specific implementation steps of both algorithms are detailed in section4.2.

3
Methodology

3.1 Introduction to data source

Table 3.1: Overview of datasets

DATA SETS		
Dataset	1	2
Source	**NASA**	**TUM**
Cathode	LCO	NCA
Number of cells	4	196
Form factor	18650	18650
Nominal Capacity	2100mAh	2500mAh
Charge Conditions	CC-CV	CC-CV
Discharge conditions	RWD	CC-CV
Temperature	Unsteady $(22 - 57°C)$	Constant $(25 - 35°C)$
Sampling	Discharging: 1 Hz charging: 1/60 Hz	Discharging & charging 1/10 Hz

3.1.1 NASA

The data set used in this study was sourced from the NASA Randomized Battery Usage Data Set. In the NASA dataset [2], batteries undergo continuous cycling through randomly generated discharge profiles under different average loads and temperatures. This data set includes data from eight different cells, all of which are 18650 lithium-ion batteries (LIBs).

3.1.1.1 Experimental Cycle and Data Recording

Each complete random walk (RW) section comprises a reference charge (standard CC-CV charge) and 50 RW discharge cycles. Each discharge cycle transitions from a state of charge (SoC) of 100% to a state of charge (SoC) of 0%, interrupted by CC-CV charging between cycles [3.5].

3.1.1.2 Calibration and Capacity Definition

Post every 50 random discharging cycles, a calibration involving a standard charge capacity test is conducted to define the true capacity. This is based on the integration of the current over time during the CC-CV charging process starting from SoC =0% until it reaches 100%. The sampling frequency for measuring the current during this process is set at 1/60 Hz, where the real capacity is determined by integrating the quantities of charge delivered during both constant - current and constant-voltage phases.

3.1.2 TUM

This report leverages an extensive dataset from an experimental degradation study of commercial Lithium-ion batteries, as documented in [1]. The dataset, contributed by Leo Wildfeuer et al., from the Technical University of Munich, encompasses the aging analysis of 196 lithium-ion cells under various operational conditions. The cells underwent comprehensive tests to simulate calendar and cycle aging processes, providing valuable insights into battery health and degradation mechanisms.

3.1.2.1 Data Structure and Availability

The data set is structured to facilitate an in-depth examination of battery degradation in wide operating conditions, showcasing the dynamic real-life situation. Includes data on capacity fade, resistance increase, and degradation modes during the battery's life cycle. The raw data, supports the development of data-driven aging models and state estimation algorithms, fostering further research in battery health management.The sampling frequency for measuring the current during this process is set at 1/10 Hz, where the real capacity is determined by integrating the quantities of charge delivered during both constant current and constant-voltage phases

3.1.2.2 Measurement of Cell Capacity

The cell capacity was determined from the raw test that had two sequential charging and discharging cycles under constant current and constant voltage (CC-CV) conditions, with parameters set at $I = 2.5A$, $U_{\max} = 4.2V$, $U_{\min} = 2.5V$, $I_{\text{cut,CV}} = 0.02C$, and $t_{\text{cut,CV}} = 1h$. Following these cycles, a charging process at a reduced rate $I = 0.25A$, $U_{\max} = 4.2V$, $I_{\text{cut,CV}} = 0.02C$, $t_{\text{cut,CV}} = 1h$ was performed to facilitate differential voltage calculation and enable half-cell fitting to identify modes of degradation.

Subsequently, to achieve the desired initial SOC for the aging studies, cells were adjusted by charging or discharging according to whether the initial SOC was above or below 20%, respectively. After completion of the CU procedures, cells were allowed to rest at an ambient temperature of 20°C before being transferred to their designated thermal chambers for subsequent cyclic or calendar aging tests. Due to limitations in resource availability and test channel access, the duration of this resting period was not strictly regulated [3].

3.1.2.3 Periodic Check ups

The cells were evaluated at constant temperature of 20°C to monitor SoH. These evaluations were called Check-Ups, which involved measuring parameters such as the cells capacity and the internal resistance which were used as one of the Health Indicators. These check-ups were essential to track the gradual changes in the cell performance over time.

3.1.2.4 The cyclic Aging

The cells were initially stored under constant conditions, which were then transferred to the thermal changes to simulate load under various temperatures and also various humidity setting, cyclic aging involved repeated charging and discharging the cells to simulate real-world battery usage. This phase is crucial for understanding how continuous usage affects the cell's performance and degradation.

3.1.2.5 Cyclic Aging conditions

The cyclic aging test had two protocols, namely Ah-based cycling and voltage-based cycling.

- **Ah based cycling** is performed by charging and discharging the cells based on their capacity. This method helps in determining the cells performance under varying charge quantities.

- **Voltage based cycling** involves setting specific voltage limits for charging and discharging the cells. This protocol ensures the effect of voltage limits on the cells performance and degradation.

These tests were carried out at different temperature 5°C, 20°C, 35°C, and 50°C. The way the cells were tested is exactly what this work aims to look at as it had all the characteristics which would get from a simulated vehicle considering that it was driven in different temperature and also at different SoC.

After the cycling the cells under go preconditioning before the checkups as mentioned in section 3.1.2.2.

3.2 Data processing

Figure 3.1: Construction of four HI and capacity labels from charging curve

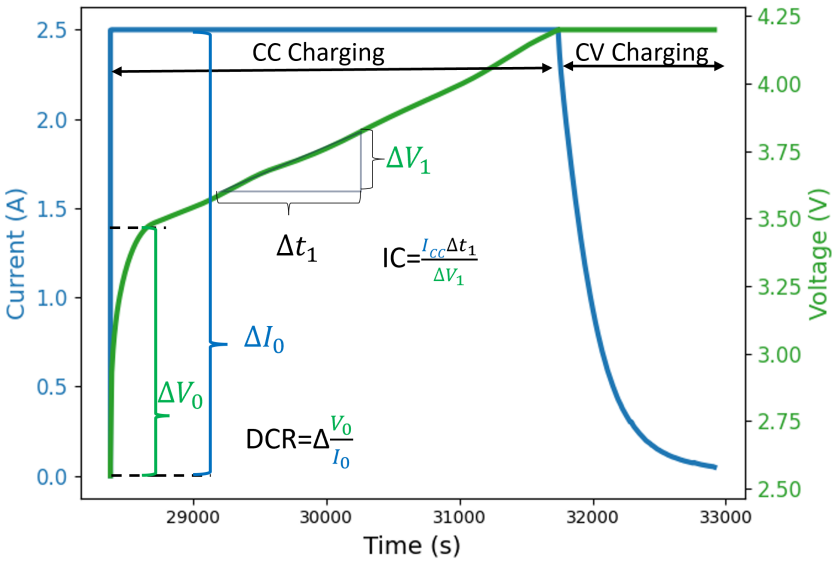

The features known as Health Indicators (HIs) are extracted from the charging cycles during checkups, as discussed in Section 3.1.2.2. The HIs and capacity labels are derived from the standard charge capacity calibration [1].

The **direct current resistance (DCR)** is one of the four health indicators (HI) computed using the initial step portion of the standard charge calibration,

$$DCR = \frac{V_{t1} - V_{t0}}{i_{t0} - i_{t1}} \tag{3.1}$$

where $t_1 - t_0 = 10\,\text{s}$. The other three features related to the Incremental Capacity (IC) also utilize data from the constant-current charging portion of the standard charge calibration,

$$IC = \frac{I_{CC}(t_2 - t_1)}{V_{t2} - V_{t1}} \tag{3.2}$$

where $t_2 - t_1 = 10\,\text{s}$. Specifically, IC_{peak} represents the peak value of the plateau. IC_{area} is the area within **20 data points** near the base of the peak value, and IC_0 represents the base point of the IC curve which is represented in figure 3.3.

The four health indicators will also be referred to as the feature henceforth. They are as follows:

- DCR
- $IC_{\mathbf{peak}}$
- $IC_{\mathbf{area}}$
- IC_0

3.2.1 Data Filtering method

After the IC analysis it is essential to clean the data to remove noise that can obscure important features. One effective method for noise reduction is the Savitzky-Golay filter.

3.2.1.1 Savitzky-Golay Filter

The Savitzky-Golay (Savgol) filter is a digital smoothing filter commonly used in data analysis to enhance the signal-to-noise ratio while preserving the essential features of the signal, such as peak heights and widths. Introduced by Abraham Savitzky and Marcel Golay in 1964, this filter operates by fitting successive sub-sets of adjacent data points with a low-degree polynomial using linear least squares. Its ability to maintain the integrity of the original signal makes it particularly useful in fields such as signal processing, analytical chemistry, and battery health diagnostics.

In our work for health diagnostics, the Savitzky-Golay filter is employed to smooth noisy data from diagnostic techniques like incremental capacity (IC) analysis. This smoothing enhances the detection of key features indicative of degradation mechanisms, leading to improved accuracy in predicting the state of health (SoH) of batteries. Thus, the Savitzky-Golay filter plays a crucial role in ensuring more reliable and efficient battery systems.

3.2.1.2 Application in IC Analysis

In this work the Savgol filter was applied to the $\frac{dQ}{dV}$ data using the following parameters:

$$\text{smoothed\_dQdV} = \text{savgol\_filter}(\text{dQdV}, \text{window\_length} = 15, \text{polyorder} = 4) \tag{3.3}$$

Parameter Justification

- **Window Length (15):** This defines the number of data points used for each polynomial fit. A window length of 15 was chosen to effectively reduces noise while preserving important features. A smaller window length may not remove enough noise, while a larger window length may oversmooth the data, losing important details.

- **Polynomial Order (4):** This is the degree of the polynomial used for fitting. A polynomial order of 4 was selected because it balances flexibility and over fitting. Higher-order polynomials can model complex data variations, but if too high, they may fit the noise instead of the actual data.

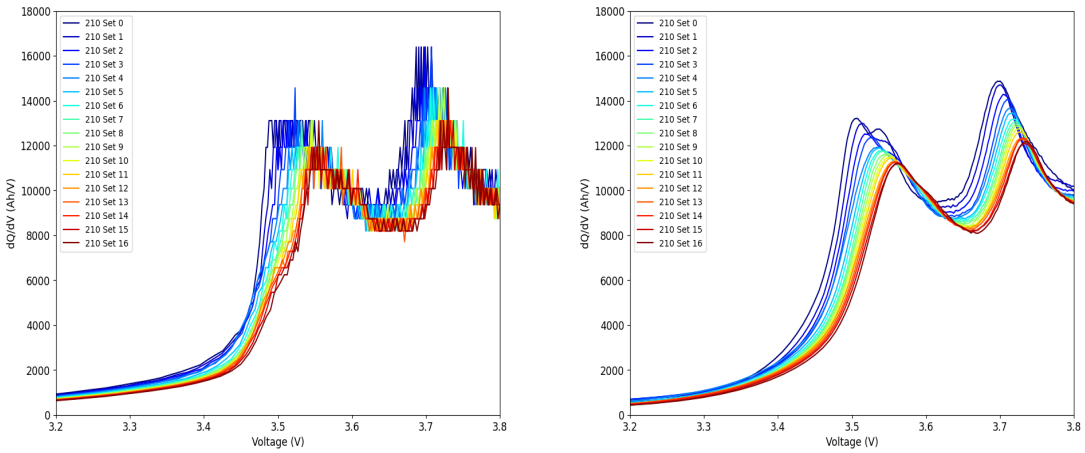

(a) Before Filtering **(b)** After filtering

Figure 3.2: Savgol filter implementation

3.2.2 Quantifying Capacity Contribution and SoH from IC analysis

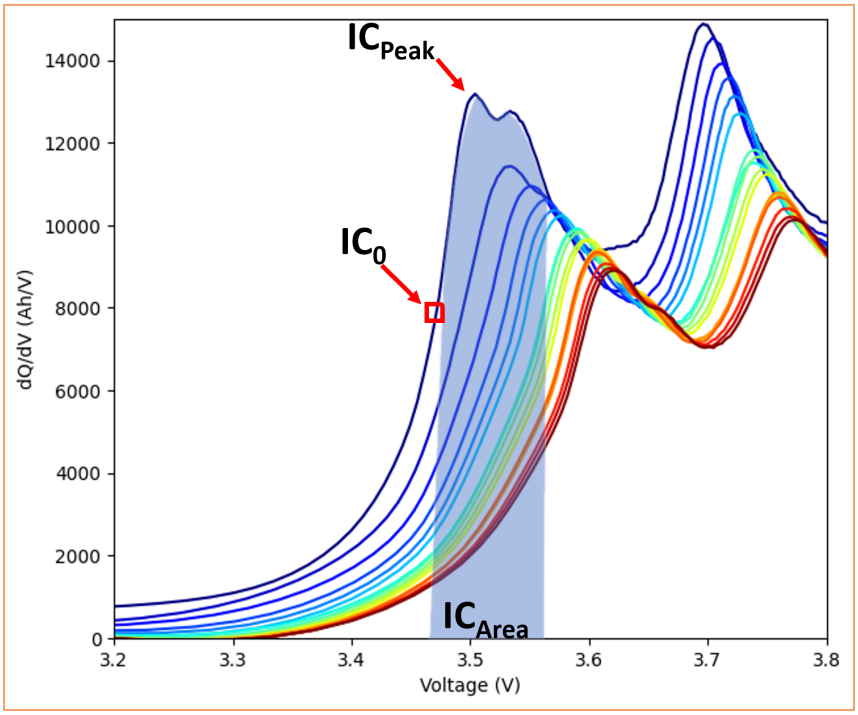

Figure 3.3: IC analysis from charging

3.2.2.1 Presence of New Peaks

The emergence of new peaks within the IC curve signifies the initiation of novel electrochemical reactions absent in a fresh cell. These reactions may stem from degradation mechanisms such as the Solid-Electrolyte Interface (SEI) layers, dissolution of electrode materials, or side reactions with the electrolyte, each contributing to the progressive decline of battery performance.

3.2.2.2 Peak Sharpness

The sharpness of peaks within the IC curve reflects phase transitions in electrode materials. Sharp peaks typically denote well-defined phase transitions, whereas broader peaks may suggest a gradual transition or inhomogeneities in the electrode material. Analyzing peak sharpness provides valuable information on the structural changes occurring within electrode materials during battery operation.

3.2.2.3 Baseline Slope and Shape

The baseline slope and shape of the IC curve, away from peak regions, offer insights into electrolyte decomposition and alterations in the battery's internal resistance. An increasing baseline slope across cycling indicates a rise in resistance or changes in electrolyte composition, both of which are critical factors in the aging process of LIBs.

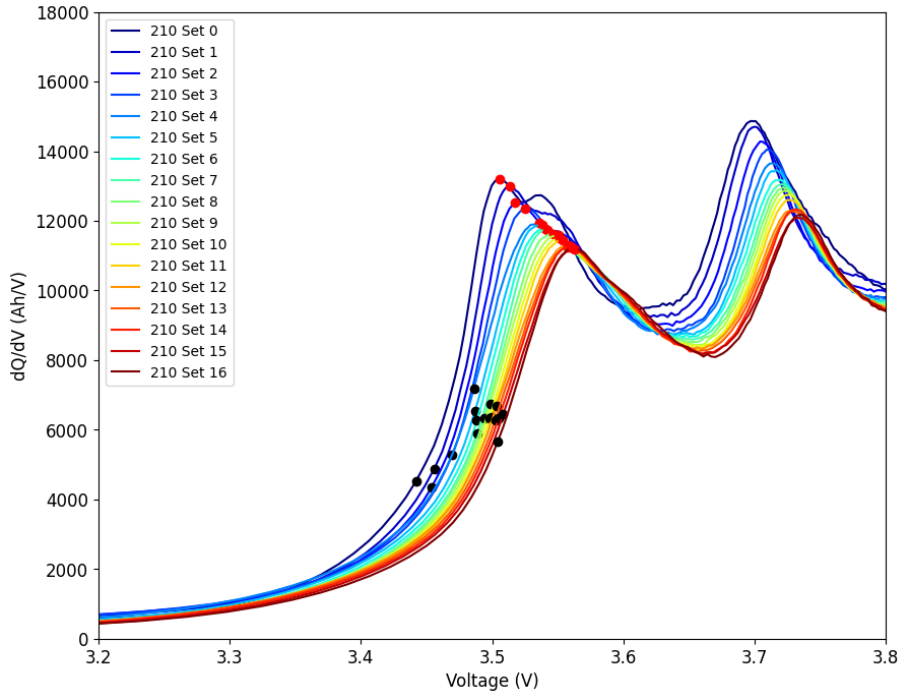

Figure 3.4: ICA on cell number 210 from TUM dataset

The figure 3.4 represents the Incremental Capacity Analysis (ICA) for cell number 210, which has been cyclically aged and checked 16 times. As shown in the figure, the peak height (red dots) fades over time, indicating the progressive loss of active

lithium ions and changes in electrode surface properties due to SEI formation. Additionally, the base level (black dots) changes, reflecting the overall capacity and efficiency degradation caused by factors such as SEI formation, lithium plating, and electrolyte decomposition. These trends highlight the impact of cyclical aging on the battery's performance.

3.2.3 Dataset normalization

Normalization is a data preprocessing technique used to scale the features of your data to a range,here we have used the limits based on the data losses we can see without distorting differences in the ranges of values. This process ensures that each feature contributes equally to the analysis, which is particularly important for algorithms.

3.2.3.1 Min-Max Scaling

Min-Max scaling is a simple and effective normalization method. It transforms the data into a fixed range, usually [0, 1], using the formula

$$X_{norm} = \frac{X - X_{min}}{X_{max} - X_{min}} \tag{3.4}$$

- where X is the original data point.
- X_{min} and X_{max} are the minimum and maximum values of the feature respectively.
- X_{norm} is the normalized data point.

This way done in order to transform features to a common scale and it maintains the relationships in the data effectively. All data sets were normalised, including the input data set, comprising the current voltage and temperature. Furthermore, the extracted health indicators were normalized, including the area under the curve, the height of the peak, and the base value of the peak. Normalisation was thus applied to all data sets.

3.2.4 Input data description

The primary datasets used in this work here include:

- **x.npy** contains normalized voltage, current, and temperature data captured during the charging cycles and the Random walk from TUM and NASA respectively[3.6][3.5].
- **y.npy** Includes extracted health indicators such as Direct Current Resistance (DCR), peak height, Area Under the Curve (AUC), and base point from the charging curves.
- **z.npy** Provides the labeled capacity values, serving as ground truth for training and validating machine learning models.

3.2.4.1 x.npy

- Dimensions: (n, T, 3)
- Description:
  - **n**: Represents the variable number of battery samples, each characterized by a sequence of charging instances.
  - **T**: Denotes the discrete time stamps captured per sample, delineating intervals during the charging process.
  - **3**: Features per time stamp:
    - **Normalized Voltage**: Reflects the electrical potential across the battery terminals.
    - **Normalized Current**: Indicates the flow of electrical charge through the battery.
    - **Normalized Temperature**: Represents the ambient temperature during the charging period.

3.2.4.2 y.npy

- Dimensions: (n, 4)
- Description:
  - **n**: Corresponds to the variable number of battery samples analyzed in x.npy.
  - **4**: Features derived from each charging curve:
    - **DCR** (Direct Current Resistance):
    - **Peak Height** IC_{Peak} .
    - **AUC**(Area Under the Curve) IC_{Area}.
    - **Base point**(IC_0).

3.2.4.3 z.npy

- Dimension: (n, 1)
- Description:
  - **n**: Corresponds to the variable number of battery samples represented in x.npy and y.npy.
  - **1**: Provides the ground truth for each battery sample, denoting the actual labeled capacity measured during testing 3.1.2.2.

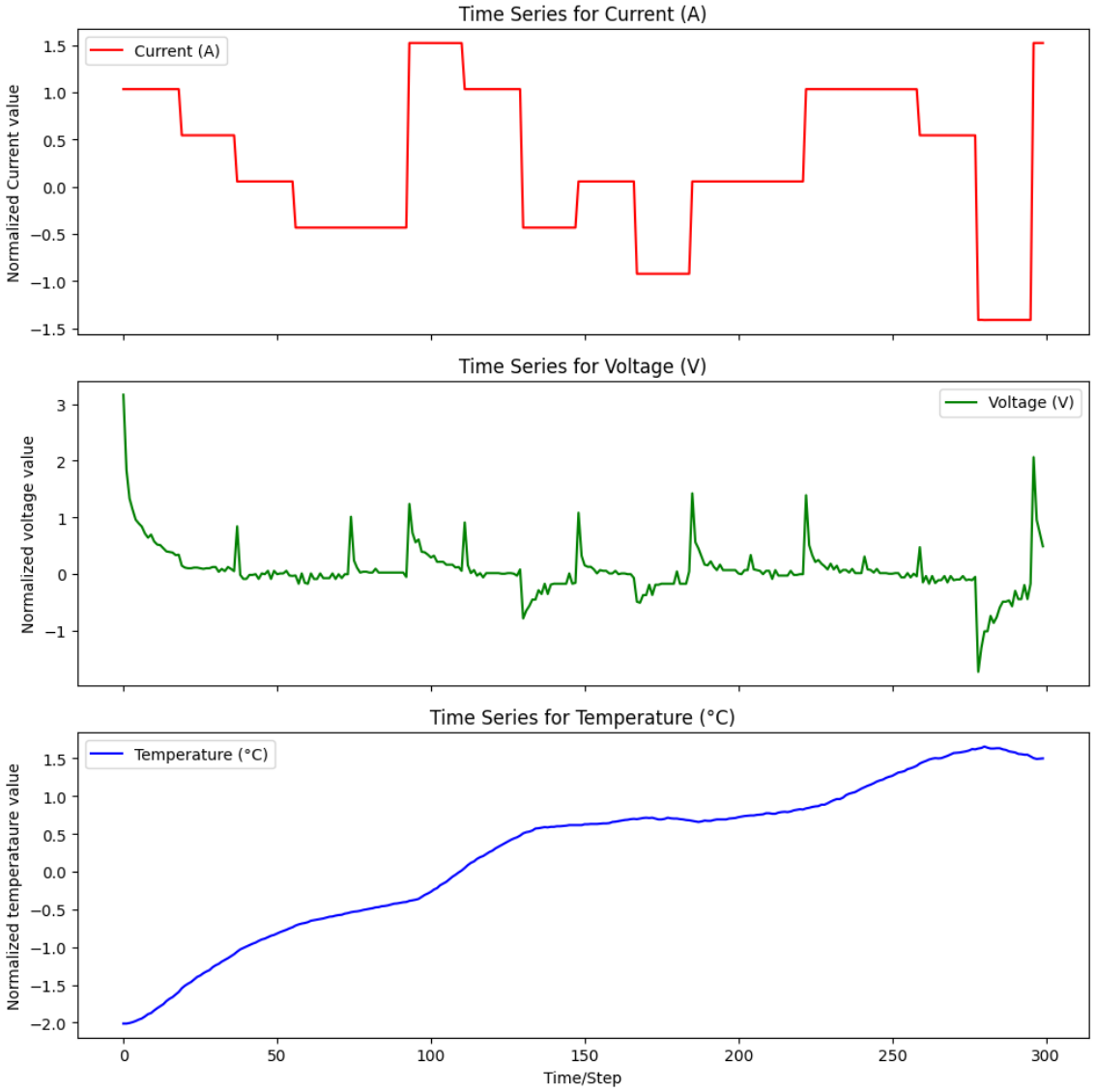

Figure 3.5: An input file x.npy is a representation of the random walk (RW) from NASA after data processing. It comprises three sections: 1. A randomly generated current profile 2. The voltage response 3. The temperature rise over time

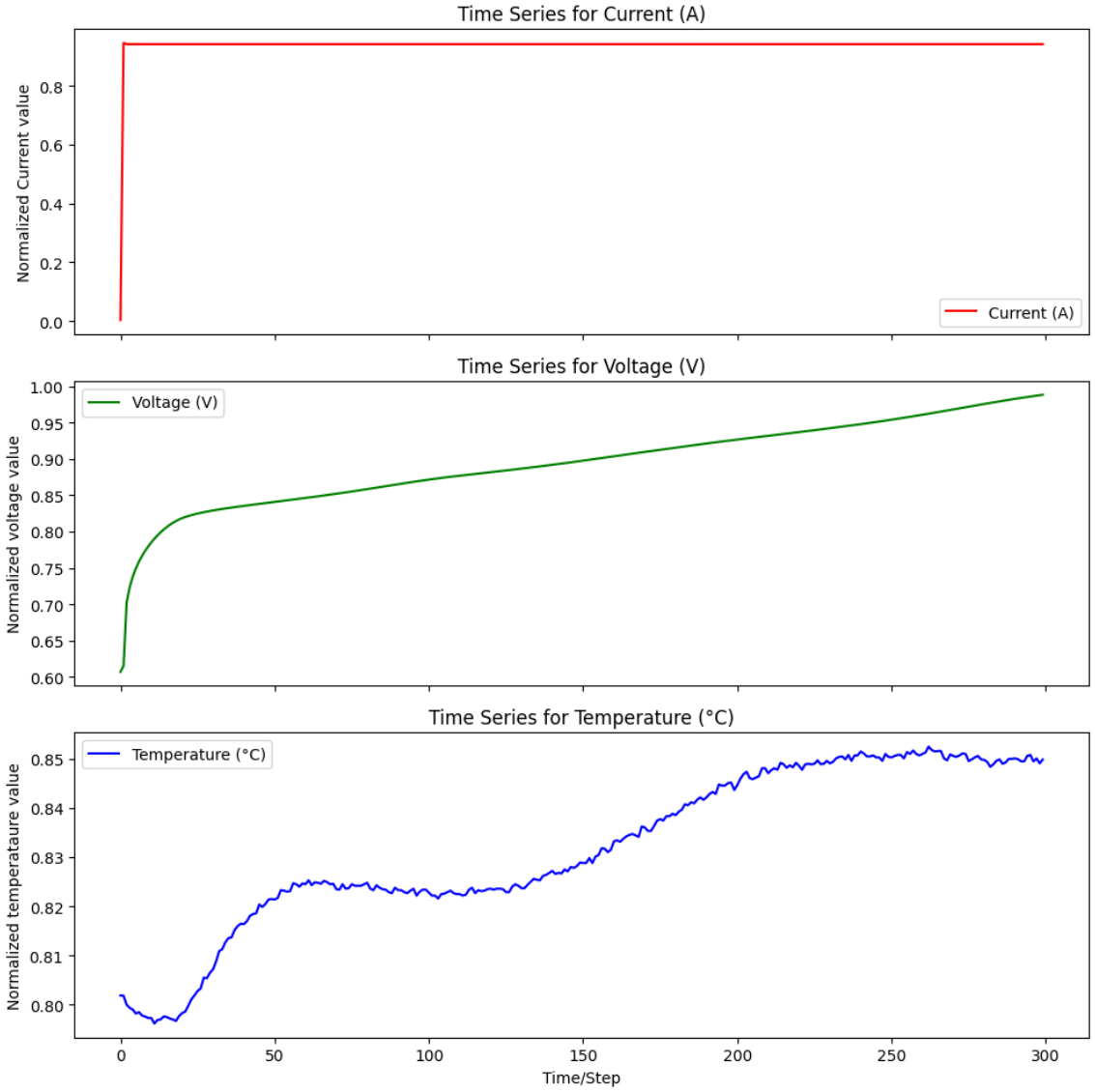

Figure 3.6: An input file x.npy is a representation of the charging cycle from TUM dataset after processing. It comprises three sections: 1. Charging current profile 2. The voltage response 3. The temperature rise over time

In Figures 3.6 and 3.5, the y-axis represents the normalised value for both datasets. The normalisation process is detailed in Section [Normalization].

4

Algorithm Implementation

4.1 Algorithm 1

BiGRU+MLP+GPR

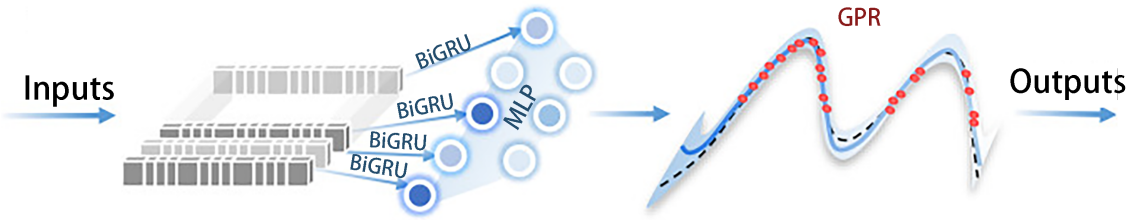

Figure 4.1: BiGRU+MLP-GPR algorithm structure
[27]

The first method is an algorithm based on BiGRU, MLP, and GPR, with its total loss function 4.3. The structure is illustrated in figure4.1, and its specific principles are as follows.

4.1.1 Upstream

The task of the upstream component is to extract capacity features from the raw battery dataset at different sampling rates, making them suitable for downstream algorithm applications. The upstream component uses partial raw battery data $\mathbf{X}$ and partially labeled battery data $\mathbf{Y}$ for supervised learning. After inputting the raw data $\mathbf{X}$ into the model, the BiGRU algorithm extracts time-based feature data from $\mathbf{X}$. These features are then mapped to four types of capacity features using the MLP algorithm. The Mean Squared Error (MSE) loss between the mapped features and the manually labeled $\mathbf{Y}$ is computed, and the feature loss is propagated downstream. The format of the input data is introduced in Section 3.2.4, with dimensions $\mathbf{X}$[n, 512, 3] and $\mathbf{Y}$[n, 4].

4.1.2 Downstream

After obtaining the four capacity features extracted upstream, the GPR algorithm is utilized to perform semi-supervised prediction of the capacity. The capacity is

regressed as a normal distribution estimate, with the mean serving as the model estimate and ±0.01 as the confidence interval. Finally, a model is obtained that can predict battery capacity based on the input of the four capacity features.

$$\text{Upstream Loss Function} = \text{MSE}(Y, \hat{Y}) = \frac{1}{n}\sum_{i=1}^{n}(Y_i - \hat{Y}_i)^2 \tag{4.1}$$

$$\text{Downstream Loss Function} = \frac{1}{n}\ln\left(p(z_L \mid Y_L, \bar{\theta})\right) + \frac{\alpha}{m}\left|\sum_{y\in Y_U} \text{Var}_{f\sim p}\left(f(y)\right)\right| \tag{4.2}$$

$$\text{Total Loss Function} = \text{Upstream Loss Function} + \text{Downstream Loss Function} \tag{4.3}$$

4.2 Algorithm 2

AE+CNN+GPR

The second algorithm is based on an autoencoder framework that employs a convolutional neural network (CNN) as the hidden layer, combined with Gaussian Process Regression (GPR). This algorithm is structured similarly to Algorithm 4.1. The primary goal of this approach is to extract effective features from the raw data $\mathbf{X}$ that can be used to predict capacity.

Initially, the algorithm utilizes an autoencoder as the upstream model to extract these features. Unlike traditional autoencoders, which typically use fully connected layers, this model integrates CNNs in the hidden layers to enhance feature extraction capabilities. When the raw data $\mathbf{X}$ is input into the upstream model, it undergoes a series of convolutional and pooling layers in the encoder. These layers are designed to capture spatial hierarchies and patterns in the data, resulting in the extraction of four distinct capacity features.

The encoder is structured to progressively reduce the dimensionality of the input data, focusing on the most relevant features for capacity prediction. Once these features are obtained, they are passed to the decoder, which consists of transposed convolutional layers (also known as deconvolutional layers). The decoder aims to reconstruct the original input data from the extracted features, thereby ensuring that the features retain essential information about the input.

To train this autoencoder, the mean squared error (MSE) between the reconstructed input and the actual input is computed. This MSE serves as the loss function for the iterative optimization process, guiding the adjustments to the weights and biases in the CNN layers. The goal of this training process is to minimize the reconstruction error, thereby ensuring the autoencoder effectively captures the most important features for capacity prediction. The specific structure of the encoder and decoder layers is detailed in section 4.1 and 4.2.

After the autoencoder has been trained and the capacity features have been extracted, these features are fed into the downstream model. This downstream model follows the same framework as the one described in Algorithm 4.1. The extracted features serve as inputs to the GPR model, which is tasked with the final capacity prediction.

While the overall framework of the upstream and downstream models in this approach mirrors that of Algorithm 1, the computation of the loss functions is handled separately. The loss functions for the upstream and downstream models are defined by the same criteria as in Algorithm 1, but they are computed independently to ensure the distinct optimization of both models. Tthe loss functions for the upstream and downstream models of this approach are computed separately, as shown in Equation 4.1 and 4.2.

By combining the feature extraction power of CNN-based autoencoders with the predictive accuracy of GPR, this algorithm aims to provide a robust method for capacity prediction, leveraging the strengths of both deep learning and statistical regression techniques.

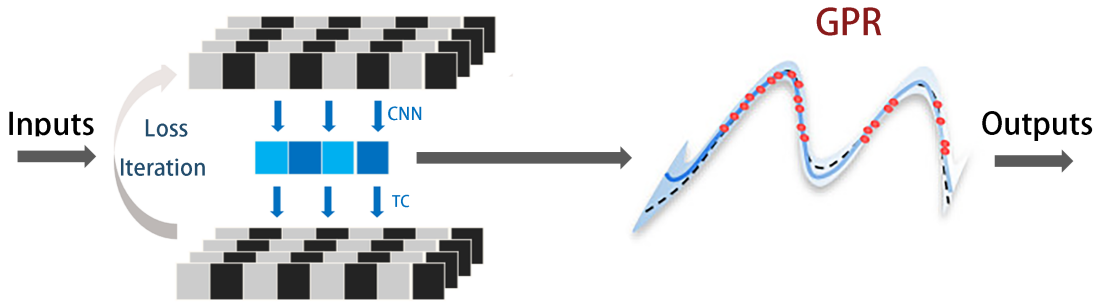

Figure 4.2: AE+CNN-GPR Algorithm structure

Table 4.1: CNN encoder Structure

Layer (type)	Input Shape	Output Shape
Convolutional Layer	3x512	16x128
Pooling Layer	16x128	16x64
Convolutional Layer	16x64	16x32
Pooling Layer	16x32	16x16
Convolutional Layer	16x16	32x16
Pooling Layer	32x16	32x8
Convolutional Layer	32x8	32x8
Convolutional Layer	32x8	4x2
Pooling Layer	4x2	4x1

Table 4.2: CNN decoder Structure

Layer (type)	**Input Shape**	**Output Shape**
Transposed Convolution layer	4x1	32x4
Transposed Convolution layer	32x4	32x8
Transposed Convolution layer	32x8	16x16
Transposed Convolution layer	16x16	16x64
Transposed Convolution layer	6x64	3x512

4.3 Evaluation indicators

To evaluate the performance of the two algorithms, MAE and RMSE are used as the main evaluation metrics.

4.3.1 Mean Absolute Error (MAE)

MAE is a measure of errors between paired observations expressing the same phenomenon. It is defined as the average of the absolute differences between predicted values and actual values,

$$\mathrm{MAE} = \frac{1}{n}\sum_{i=1}^{n}|y_i - \hat{y}_i| \tag{4.4}$$

- n is the number of observations,
- y_i is the actual value,
- $\hat{y}_i$ is the predicted value.

4.3.2 Root Mean Square Error (RMSE)

RMSE is a quadratic scoring rule that also measures the average magnitude of error. It is the square root of the average of squared differences between predicted and actual values,

$$\mathrm{RMSE} = \sqrt{\frac{1}{n}\sum_{i=1}^{n}(y_i - \hat{y}_i)^2} \tag{4.5}$$

- n is the number of observations,
- y_i is the actual value,
- $\hat{y}_i$ is the predicted value.

5
Results

This chapter presents the model's results, including findings from testing on the NASA and TUM datasets. Section 4.1 compares the performance of Algorithm 1 [4.1] and Algorithm 2 [4.2] under identical conditions. Section [5.2] analyzes the influence of different Hyperparameters s on the performance of these algorithms.

5.1 Results under standard condition

Table 5.1: Hyperparameter settings

Hyperparameter	**Setting**
Learning rate	0.01
Optimizer	Adam
Number of training epochs	30
Number of batteries for train	6
Number of batteries for test	2
Number of hidden layers	5, 14
GPR Kenel	RBF Kernel

To objectively compare the performance of both algorithms, it is essential to evaluate them under identical conditions. Therefore, model is trained and tested both using the same set of hyperparameters, and then compare the results obtained. The hyperparameter settings are detailed in the table 5.1. All results reported here are based on computations performed using one RTX 1080Ti GPU.

5.1.1 RMSE and MAE results

Table 5.2: Results based on BiGRU+MLP+GPR algorithm

	Up RMSE	Up MAE	Down RMSE	Down MAE	computational time
NASA	0.432	0.328	0.301	0.238	23s
TUM	0.262	0.191	0.109	0.075	16s

Table 5.3: Results based on AE+CNN+GPR algorithm

	RMSE	MAE	computational time
NASA	0.524	0.412	167s
TUM	0.097	0.075	161s

Table 5.4: Results based on BiGRU+MLP+GPR algorithm

	Up RMSE	Up MAE	Down RMSE	Down MAE	computational time
NASA	0.427	0.317	0.30	0.238	23s
TUM	0.262	0.191	0.109	0.07	16s

5.1.2 NASA dataset

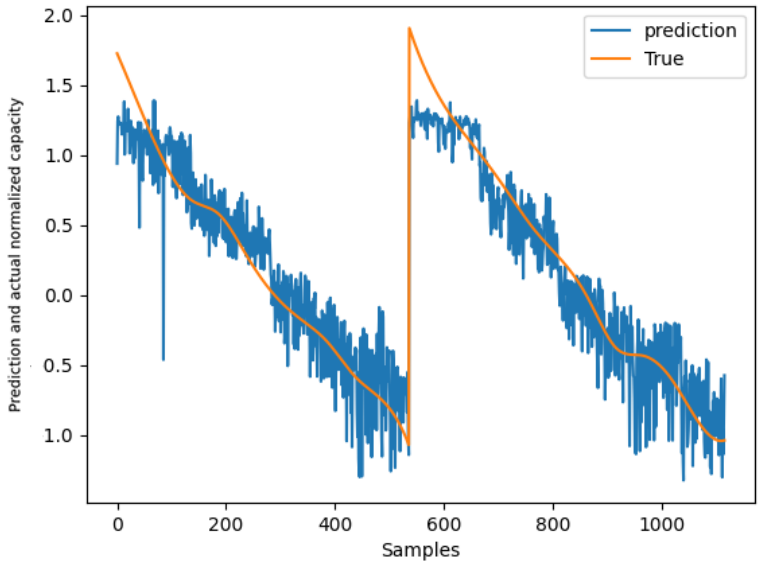

Figure 5.1: BiGRU+MLP+GPR based capacity estimation

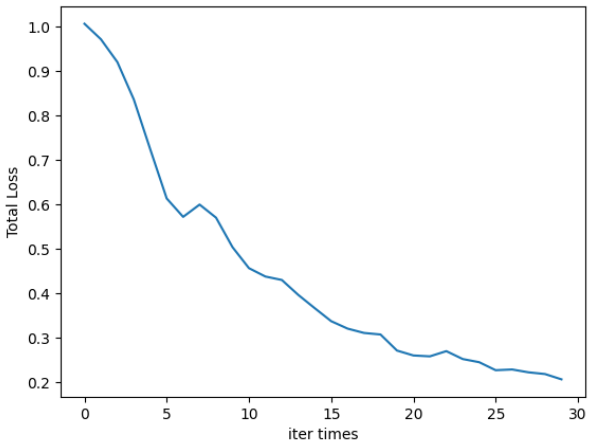

Figure 5.2: Upstream loss

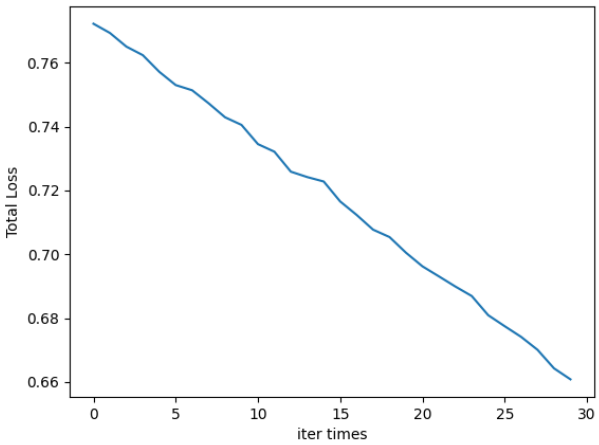

Figure 5.3: Downstream loss

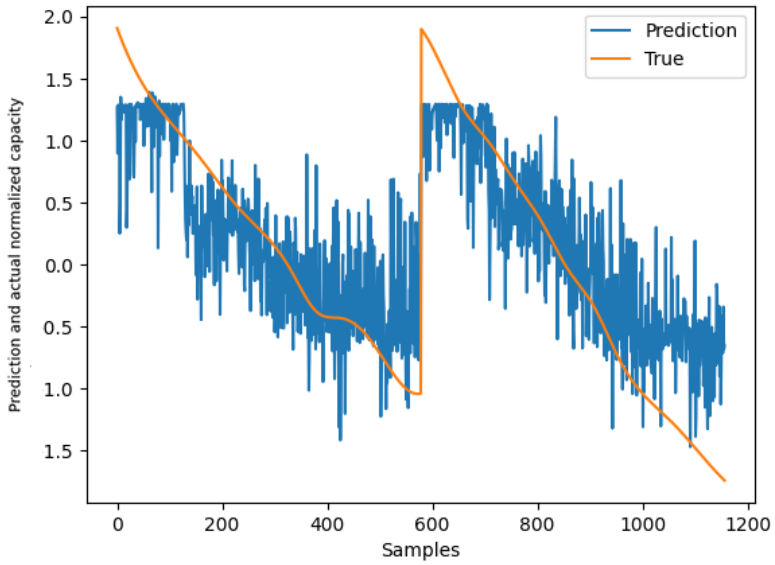

Figure 5.4: AE+CNN+GPR based estimated capacity

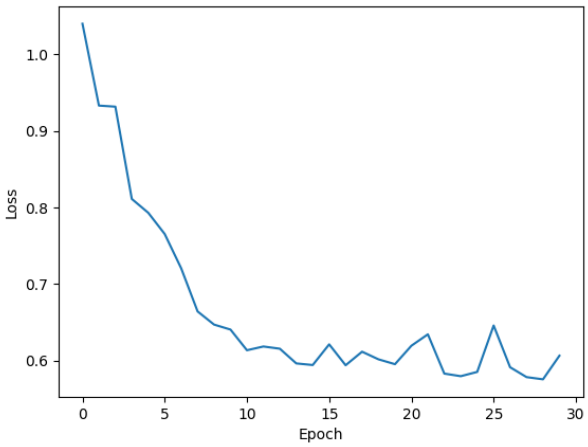

Figure 5.5: Upstream loss

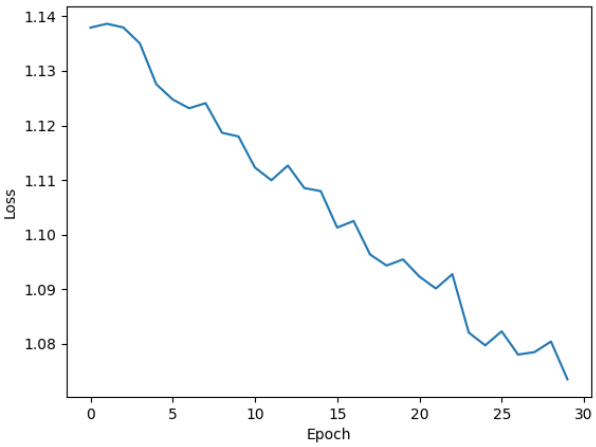

Figure 5.6: Downstream loss

5.1.3 TUM dataset

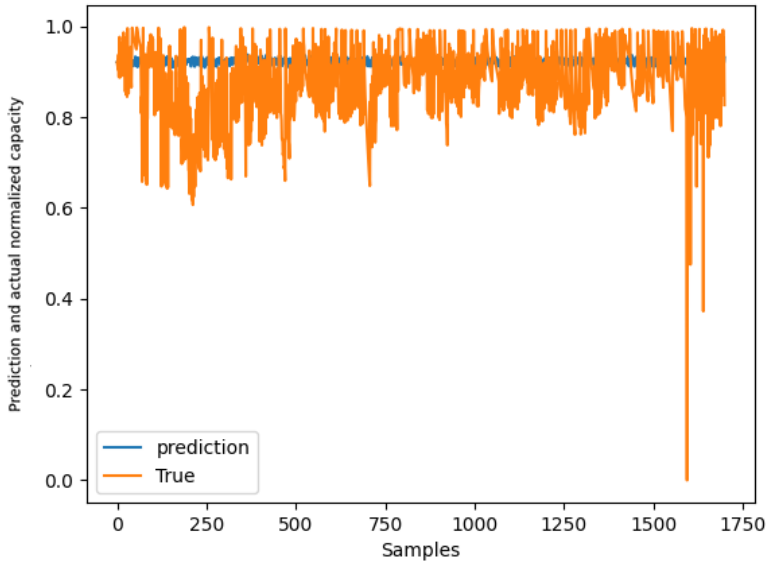

Figure 5.7: BiGRU+MLP+GPR based capacity estimation

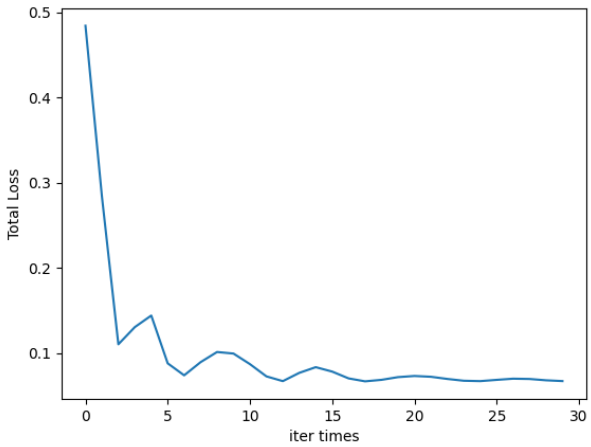

Figure 5.8: Upstream loss

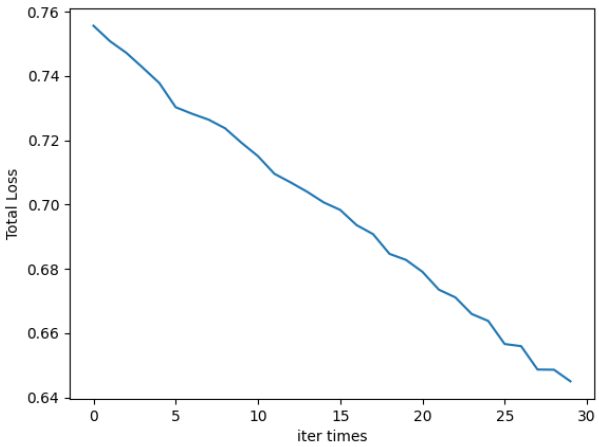

Figure 5.9: Downstream loss

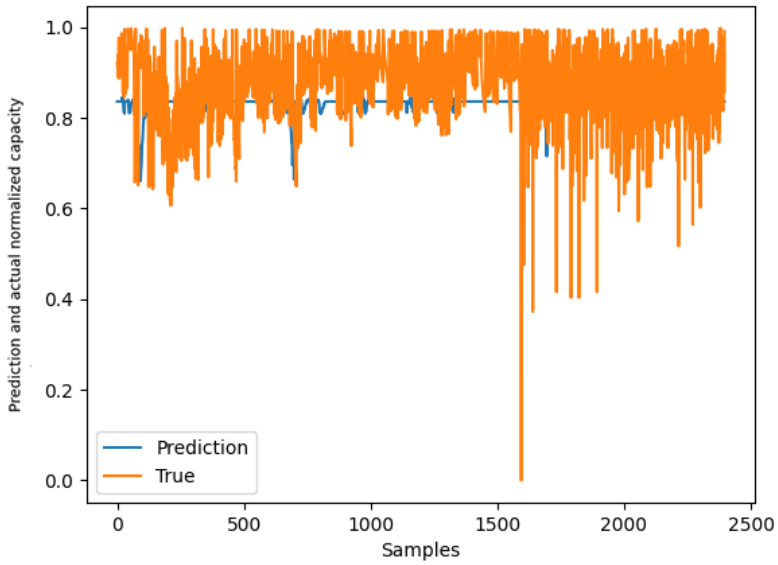

Figure 5.10: AE+CNN+GPR based capacity estimation

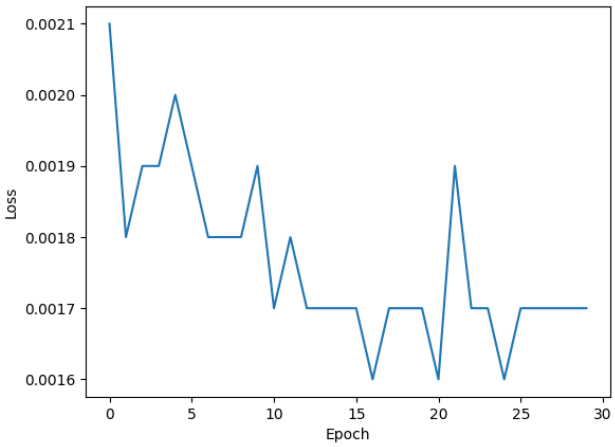

Figure 5.11: Upstream loss

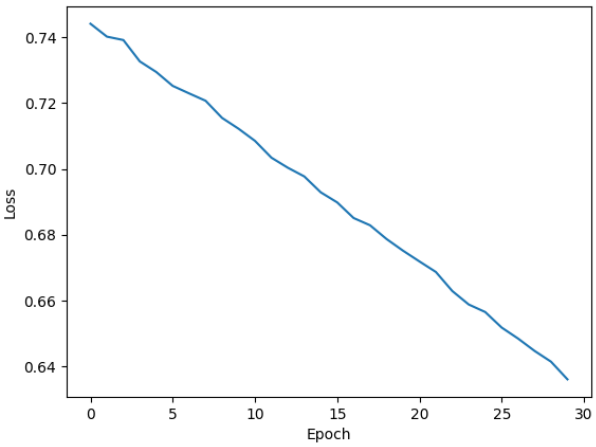

Figure 5.12: Downstream loss

The results of the two algorithms are shown in Table 5.4 and Table 5.3. On the NASA dataset, the BiGRU+MLP+GPR algorithm has 57% of the RMSE and 58% of the MAE of the AE+CNN+GPR algorithm. In terms of transit time count BiGRU+MLP+GPR takes 21% of the time of AE+CNN+GPR algorithm. On the TUM dataset, its RMSE and MAE are not cross-referenced because they deviate too much from the original dataset, and their visualisation is shown in Figure 5.7 and Figure 5.10.

The prediction results of the two algorithms on the NASA dataset are shown in Figure 5.1 and Figure 5.4, where it can be seen that the performance of the BiGRU+MLP+GPR algorithm's fit improves with the number of samples from both batteries, reaching the best performance at the 240 sample.

The AE+CNN+GPR algorithm exhibits more pronounced oscillations compared to the former approach. Notably, the predictions for the initial 75-100 sampling points of the cell do not align with the trend of the true capacity. The algorithm reaches its optimal performance around the 200th sampling point. Beyond this point, the predicted oscillations increase significantly, particularly in the second half of the battery samples.

It can be seen from Figure 5.2 and Figure 5.3 that the upstream loss of the BiGRU+MLP+GPR algorithm has the fastest rate of loss reduction in the first 10 iterations, and it finally stabilises after 25 iterations. While the AE+CNN+GPR algorithm algorithm tends to stabilise after the tenth iteration and shows signs of overfitting. Figure 5.5 and Figure 5.6 show that the loss of the two algorithms in the downstream GPR algorithm species shows a similar linear variation with the number of iterations.

5.2 Hyperparameters Analysis

Further investigations were conducted to determine the impact of different hyperparameter variations on model performance, with a particular focus on changes in model accuracy and loss. Initially, benchmark tests were conducted to assess the impact of varying the number of training layers based on modifications to upstream and downstream losses. Subsequently, the effects of utilising different Gaussian kernels downstream on algorithm performance were examined. Finally, the robustness of the algorithm was evaluated through the introduction of Gaussian white noise. All benchmarks were conducted using the NASA battery dataset.

5.2.1 Comparison of different training epochs

5.2.1.1 BiGRU+MLP+GPR algorithm

Table 5.5: RMSE and MAE results

Epochs	RMSE	MAE
50	0.345	0.263
100	0.328	0.252
150	0.298	0.221
200	0.317	0.241

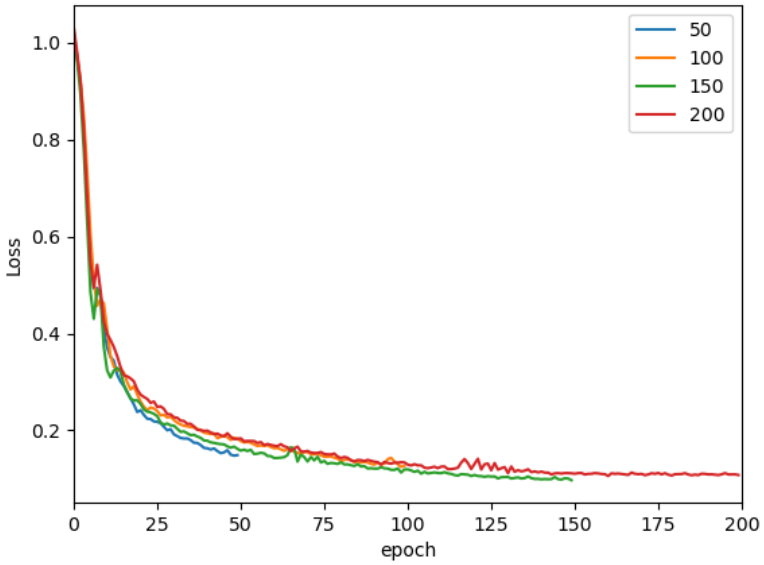

Figure 5.13: Variation of loss with different number of training epochs

5.2.1.2 CNN+AE+GPR algorithm

Table 5.6: RMSE and MAE results

Epochs	RMSE	MAE
15	0.536	0.418
50	0.509	0.399
75	0.506	0.397
100	0.5	0.393

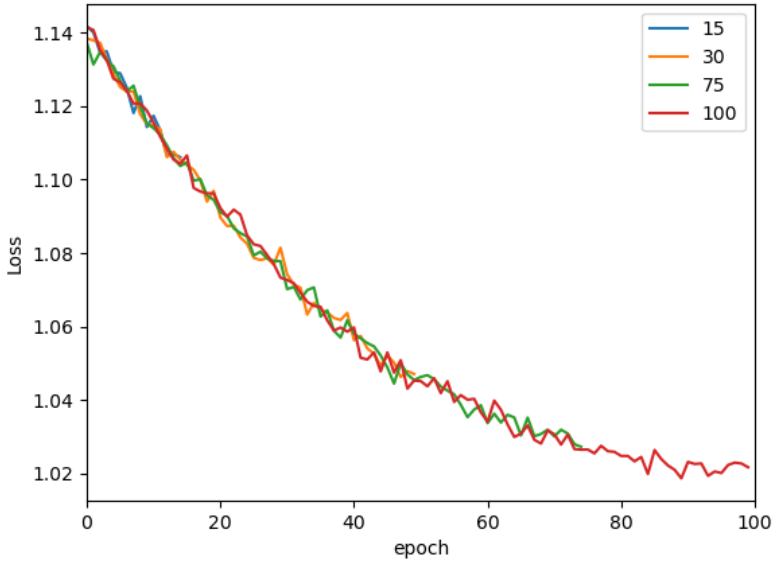

Figure 5.14: Variation of loss with different number of training epochs

Through previous benchmark tests, it was found that the BiGRU+MLP+GPR algorithm did not show overfitting similar to AE+CNN+GPR before 30 iterations, so in order to test the best performance of the algorithm upstream. the performance was tested of the algorithm's upstream function in different 50 to 250 epochs respectively, and the results are shown in Figure 5.13, which shows that in the first 25 layers of iteration kind of loss decreases rapidly, and the decrease gradually slows down in 25 to 75 iterations, and after 75 iterations, the loss decreases tends to level off, and there are signs of overfitting. The overfitting phenomenon after 150 layers can also be seen from Table 5.5.

In the AE+CNN+GPR algo rithm it was found that the upstream of the algorithm started to overfit linearly after 10 iterations, so the upstream was frozen to see how the downstream performs after more iterations, and the results are shown in Figure 5.14, where the loss shows a similarly linear decrease in the first 80 iterations, and the loss starts to overfit after 80 iterations. Comparing the RMSE and MAE in Table 5.6 we can see that the RMSE decreases by 5.0% after the number

of iterations changes from 15 to 50. After that the decrease in RMSE from 50 to 100 iterations levelled off at 0.6% versus 1.2%. MAE changes have the same trend as RMSE.

5.2.2 Computational results based on different downstream Gaussian kernels

Due to variations in flexibility and smoothness among different Gaussian kernels, and the dynamic nature of the mapping between capacity features in battery datasets and battery degradation, the performance were evaluated on three Gaussian kernels across two algorithms.

5.2.2.1 Kernel results based on BiGRU+MLP+GPR

Table 5.7: RMSE and MAE results on NASA dataset

	RMSE	MAE
RBF Kernel	0.294	0.235
RQKernel	0.381	0.312
Matern Kernel	0.425	0.321

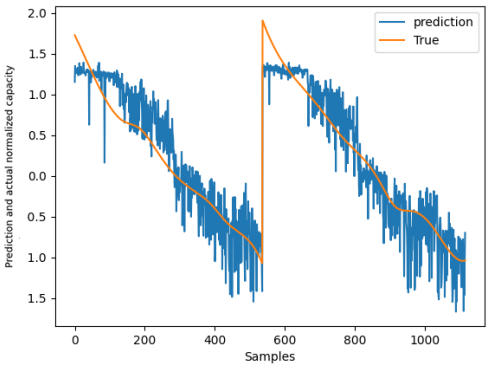

Figure 5.15: RBFKernel

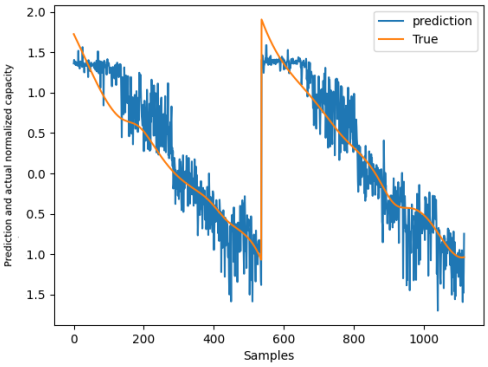

Figure 5.16: RQKernel

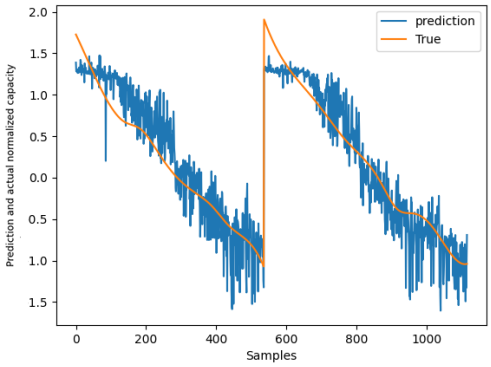

Figure 5.17: Matern Kernel

Table 5.8: RMSE and MAE results on TUM dataset

	RMSE	MAE
RBF Kernel	0.087	0.063
RQKernel	0.086	0.066
Matern Kernel	0.090	0.063

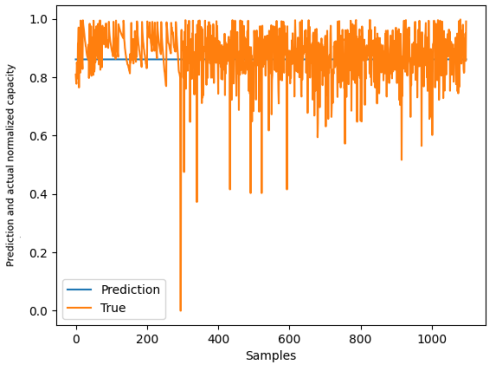

Figure 5.18: RBF Kernel

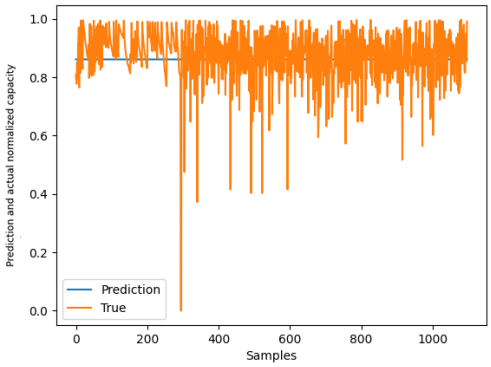

Figure 5.19: RQKernel

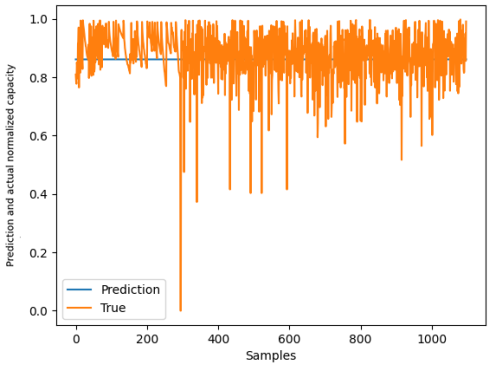

Figure 5.20: Matern Kernel

5.2.2.2 Kernel results based on AE+CNN+GPR

Table 5.9: RMSE and MAE results on NASA dataset

	RMSE	MAE
RBFKernel	0.524	0.409
RQKernel	0.494	0.386
MaternKernel	0.521	0.409

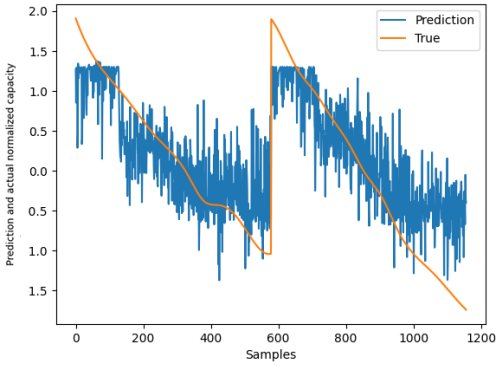

Figure 5.21: RBF Kernel

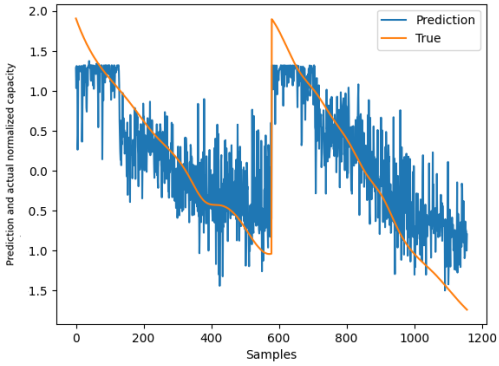

Figure 5.22: RQKernel

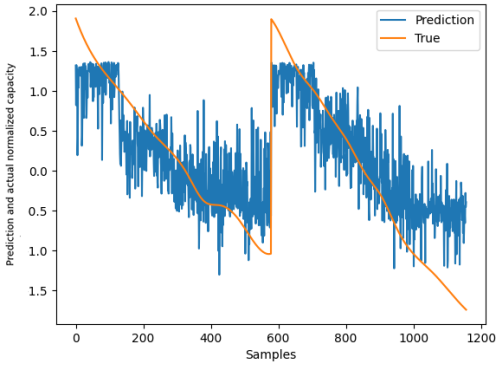

Figure 5.23: Matern Kernel

Table 5.10: RMSE and MAE results on TUM dataset

	RMSE	MAE
RBF Kernel	0.091	0.065
RQKernel	0.091	0.065
Matern Kernel	0.091	0.065

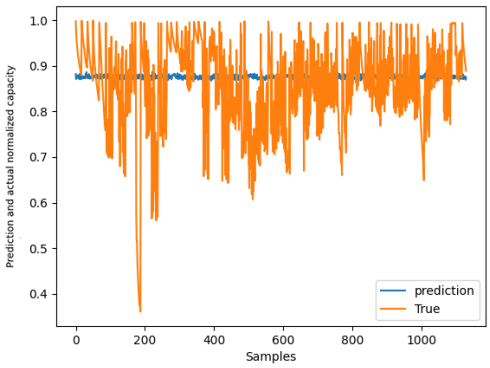

Figure 5.24: RBF Kernel

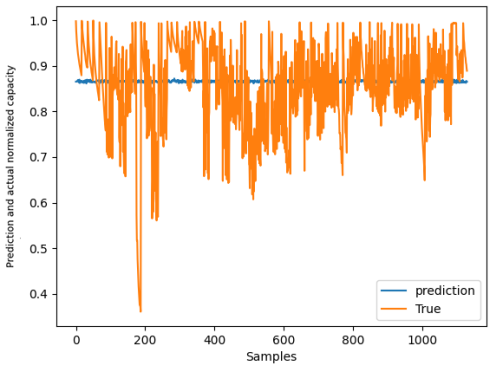

Figure 5.25: RQKernel

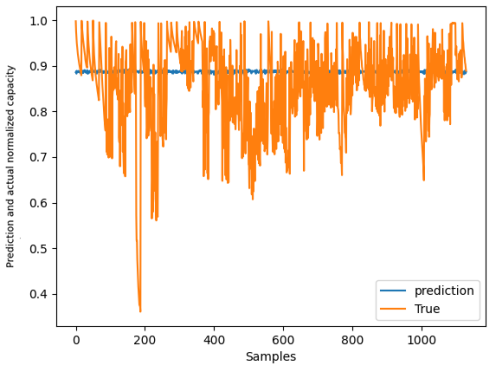

Figure 5.26: Matern Kernel

Table 5.7 and 5.9 shows that RBF kernel has the best RMSE and MAE performance in BiGRU+MLP+GPR algorithm. The RQKernel kernel has the best RMSE and MAE performance in the AE+CNN+GPR algorithm. From the prediction line graphs of the two algorithms, it is evident that the three kernels are similar to the benchmark test 5.1 in terms of predicting trends and changes, and do not show much difference.

In the TUM dataset results 5.8 and 5.10, the predictive model exhibited poor performance in fitting the real data, significantly deviating from the observed values. Specifically, there was a substantial discrepancy between the model's predicted values and the actual measurements. Residual analysis indicated the presence of systematic bias in the error distribution, suggesting that the model fails to effectively capture the nonlinear characteristics of the data.

5.2.3 Performance of algorithms in the presence of noise

To simulate the measurement errors in battery data collection realistically and evaluate the robustness of algorithms, Gaussian noise was added with a range of $\pm 10\%$ to the original battery dataset $\mathbf{X}$. Below are the performance results of the two algorithms on the NASA dataset after applying this noise.

Table 5.11: Algorithm results under noise conditions on NASA dataset

Algorithm	RMSE	MAE
BiGRU+MLP+GPR	0.374	0.304
AE+CNN+GPR	0.542	0.429

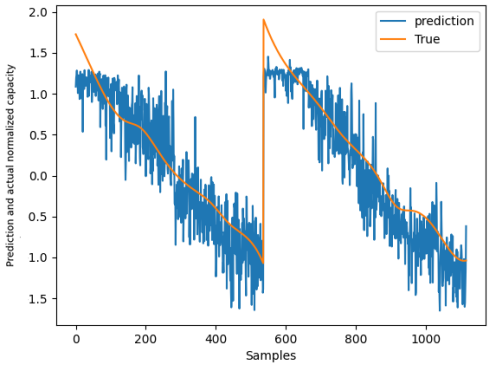

Figure 5.27: Results on BiGRU+MLP+GPR

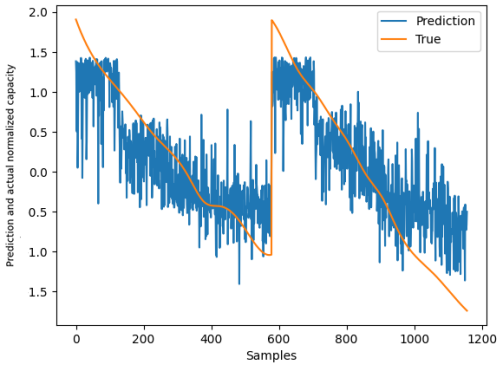

Figure 5.28: Results on AE+CNN+GPR

Table 5.12: Algorithm results under noise conditions on TUM dataset

Algorithm	RMSE	MAE
BiGRU+MLP+GPR	0.1005	0.0675
AE+CNN+GPR	0.091	0.0654

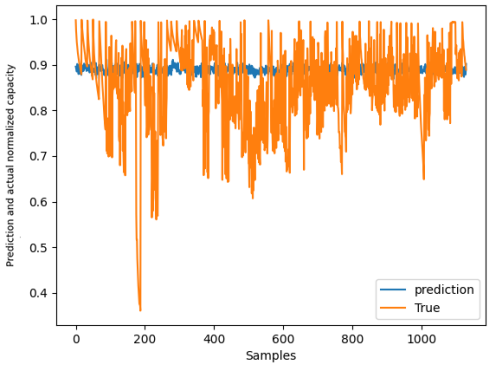

Figure 5.29: Results on BiGRU+MLP+GPR

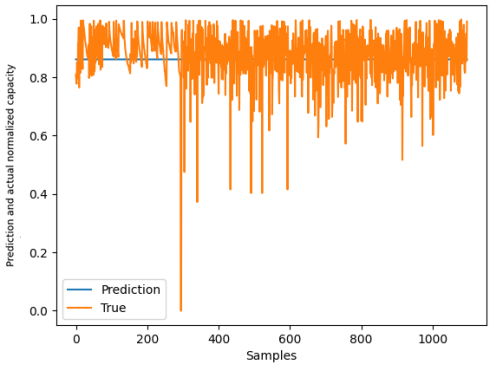

Figure 5.30: Results on AE+CNN+GPR

As can be seen from Table 5.11, with the same hyperparameters as 5.1, the RMSE of the BiGRU+MLP+GPR algorithm with ±10% Gaussian noise is 124.3% of the original and the MAE is 127.7% of the original.The RMSE of the AE+CNN+GPR

algorithm is 103.6% of the original and the MAE is 4.8% of the original. From Figure 5.27 and Figure 5.28 it can be seen that the two algorithms do not change much in predicting the trend.

In the TUM dataset 5.12, RMSE and MAE are higher than the standard state but the predictive model still fails to effectively capture the nonlinear characteristics of the data.

6
Conclusion

6.1 Results from Present Work

This thesis focused on developing and evaluating deep learning algorithms for battery capacity diagnosis, specifically comparing the performance of two algorithms BiGRU+MLP+GPR and AE+CNN+GPR, using NASA and TUM datasets. The research aimed to determine the effectiveness of these algorithms under various conditions and identify the influence of different variables on their performance.
The key findings of this research are summarized in this chapter.

6.1.1 Algorithm Comparison

Both algorithms were trained and tested under identical conditions with the same set of hyperparameters. The BiGRU+MLP+GPR algorithm consistently outperformed the AE+CNN+GPR algorithm on the NASA dataset, achieving 57% of the RMSE and 58% of the MAE compared to AE+CNN+GPR. Additionally, BiGRU+MLP+GPR demonstrated superior computational efficiency, taking only 21% of the time required by AE+CNN+GPR.

6.1.2 Performance on Battery Datasets

The performance on the TUM dataset was poor due to significant deviations from the original dataset. On the NASA dataset, as the number of samples increased, the prediction accuracy of both algorithms improved significantly. However, oscillations were observed in the predictions towards the end of the sample range.
Influence of Hyperparameters on Algorithms: Regarding the number of training epochs, the BiGRU+MLP+GPR algorithm achieved optimal performance upstream at 75 iterations, while the loss for the AE+CNN+GPR algorithm stabilized after the tenth iteration. In terms of Gaussian kernel selection, the RBFKernel provided the best RMSE and MAE for the BiGRU+MLP+GPR algorithm, whereas the RQKernel offered the best performance for the AE+CNN+GPR algorithm.
When it comes to noise Robustness both the algorithms maintained trend predictions under the addition of Gaussian noise. However, the RMSE and MAE of the BiGRU+MLP+GPR algorithm increased by 124.3% and 127.7%, respectively, while the RMSE and MAE of the AE+CNN+GPR algorithm increased by 103.6% and 104.8%, respectively.

6.1.3 Impact of Sampling Frequency on Algorithm Performance

One of the critical findings from this study was the impact of the sampling frequency on the performance of the algorithm, particularly when comparing the results from the NASA and TUM datasets.

The NASA dataset has a sampling frequency of 1/60Hz, providing a higher resolution of data points over time. In contrast, the TUM dataset has a much denser sampling frequency 1/10Hz. This discrepancy in sampling frequency significantly influenced the algorithm performance, leading to poorer results with the TUM dataset. The primary reasons for this are as follows.

Data Density and Redundancy

- The TUM dataset's denser sampling frequency results in a larger number of data points over a short period. While having more data can generally be beneficial, in this case, the high density of data points can introduce redundancy. This redundancy can overwhelm the model, making it difficult to extract meaningful patterns and trends from the data. The algorithm struggles to differentiate between noise and actual signal variations, leading to less accurate predictions.

Model Training and Overfitting

- With an excessive number of data points, there is a risk of the model over fitting to the training data. Overfitting occurs when the model learns not just the underlying patterns but also the noise and random fluctuations present in the dense dataset. As a result, the model performance well on the training data but poorly on unseen test data. the TUM dataset's higher sampling frequency faces this issue, leading to sub optimal generalization and reduced accuracy in real world applications.

Computational Efficiency

- The processing of a substantial number of data points increases the computational load on the algorithm. The dense data from the TUM dataset necessitates greater processing power and time for training, which can be inefficient and impractical, particularly in environments with limited resources. This augmented complexity can further impair the performance of the algorithms, as they must allocate more resources to manage the dense data.

In accordance with the objectives of this study, the following conclusions were reached. Initially, the four extracted features demonstrated a notable correlation with battery capacity, indicating their considerable potential for application in battery capacity prediction. Furthermore, the incorporation of additional features will enhance the accuracy of the prediction. The algorithm built upon these features

demonstrated strong accuracy and computational efficiency in predicting battery capacity (SoH). However, the performance of batteries on different datasets varies greatly. For different types of datasets, further data sampling and preprocessing are recommended before deploying the algorithm. Additionally, in the two algorithms used, hyperparameters (such as kernel selection) had varying impacts on performance. Therefore, hyperparameter settings should be optimized and adjusted according to the specific characteristics of the battery datasets and prediction requirements to enhance the model's predictive capabilities.

6.2 Future Work

The result of this research demonstrate the significant potential of deep learning algorithms in battery capacity diagnosis. However, several areas warrant further exploration to enhance performance and applicability. Below are the proposed objective for the future work.

- **Dataset Expansion** To developer more robust machine learning model and enhance the generalization of out algorithms across various battery chemistry and usage conditions, it is essential to expand the datasets used for training and testing. Incorporating more diverse and larger datasets will enable the model to be more resilient to different operational scenarios.

  - Collecting and integrating datasets from a wider range of sources, including different battery chemistry's and operational environments.

  - Utilizing open source datasets from institutions like Stanford and SNL to transition towards a big data analytical framework, which will enhance our capacity to derive more features from more data.

- **Real-World Testing**
  To asses the practical applicability and reliability of out developed algorithms, it is Cruise to implement them in real-world battery management systems and conduct extensive field testing. This will provide valuable insights into their performance in various operational scenarios and help identify areas for important.

  - Collaborating with industry partners to test the algorithms in commercial battery management systems.

  - Gathering real-world performance data to validate and refine the models.

- **Algorithm and Script Enhancement** Continuous improvement of the feature extraction capabilities of out scripts is an ongoing priority. This refinement process directly influences the efficiency and effectiveness of our diagnostics system.

  - Enhancing existing algorithms to improve their accuracy and computational efficiency.

  - Developing new algorithms that can better handle the complexities of battery health diagnostics.

- **Big Data Integration** Transitioning towards a big data analytics framework is a key objective, as it will significantly enhance our ability to derive meaningful insights from extensive datasets.

  - Implementing scalable data processing and analysis infrastructure to handle large volumes of data efficiently.

  - Utilizing advanced data mining techniques to extract more hidden patterns and trends in battery performance data.

  - Collaborating with academic and industry partners to share data and insights.

7

Ethical and Sustainability concern

In context of this work, ethical considerations are paramount, particularly when utilizing open-source data for training machine learning models. The ethical use of data involves ensuring that the data collected and used respects privacy and is free from biases that could lead to unfair outcomes. For instance, when working with the data from diverse sources, it is essential to verify that the data accurately represents the range of real world conditions and does not inadvertently favour or disadvantage any specific type of battery or use case. Transparency in how data is collected, processed and used in the diagnostics algorithms is critical. By clearly documenting and communicating these processes the system can be trusted and is operated ethically and fairly, aligning with the broader principles of fairness, accountability and transparency as outlined in the European approach to AI [28].

Sustainability in battery health diagnostics not only relates to the technical robustness and efficiency of the AI model but also extends to the environmental and social impact of the solutions developed. By using open-source data, the research promotes resource efficiency, as it avoids the need for redundant data collection efforts and encourages collaborating across the global research community. Additionally, the development of accurate and reliable battery health diagnostics supports sustainability by extending the lifespan of batteries in electric vehicle and renewable energy systems, thereby reducing waste and the demand for raw materials. This approach aligns with the principles of well being and sustainability development by contributing to the broader adoption of environmentally friendly technologies, thus supporting global efforts to mitigate climate and promote sustainable energy practices.

Bibliography

[1] Wildfeuer, L., Karger, A., Aygül, D., Wassiliadis, N., Jossen, A., and Lienkamp, M. (2023). Experimental degradation study of a commercial lithium-ion battery. Journal of Power Sources, 560, 232498. https://doi.org/10.1016/j.jpowsour.2022.232498.

[2] Bole, B., Kulkarni, C., and Daigle, M. (2014). Randomized battery usage data set. NASA Ames Progn. Data Repos, 70.

[3] Wildfeuer, L. et al. (2023). Experimental degradation study of a commercial lithium-ion battery. Journal of Power Sources, 560, 232498. https://doi.org/10.1016/j.jpowsour.2022.232498.

[4] Tarascon, J.-M., and Armand, M. (2001). Issues and challenges facing rechargeable lithium batteries. Nature, 414(6861), 359-367. https://doi.org/10.1038/35104644.

[5] Theuerkauf, D., and Swan, L. (2022). Characteristics of Open Circuit Voltage Relaxation in Lithium-Ion Batteries for the Purpose of State of Charge and State of Health Analysis. Batteries, 8, 77. https://doi.org/10.3390/batteries8080077.

[6] Li, R. et al. (2023). Lithium-ion battery degradation: using degradation mode analysis to validate lifetime prediction modelling. [Journal Name], [Vol], [Num], [Pages]. https://doi.org/10.48550/arXiv.2311.05482.

[7] Luo, G., Zhang, Y., and Tang, A. (2023). Understanding the impact of temperature on lithium-ion battery health and performance. Energies, 16(10), 4232. https://doi.org/10.3390/en16104232.

[8] O'Kane, S. E. J., Ai, W., Madabattula, G., Alonso-Alvarez, D., Timms, R., Sulzer, V., Edge, J. S., Wu, B., Offer, G. J., and Marinescu, M. (2022). Lithium-Ion Battery Degradation: How to Model It. https://doi.org/10.1039/D2CP00417H.

[9] Zhang, Y. (2023). Data-driven battery aging diagnostics and prognostics: for automotive applications. Department of Electrical Engineering, Chalmers University of Technology. https://research.ebsco.com/c/lu54te/search/

details/lbwpdgs4c5.

[10] An Overview on Thermal Safety Issues of Lithium-ion Batteries for Electric Vehicle Application - Scientific Figure on ResearchGate. Available from: https://www.researchgate.net/figure/Schematic-of-the-Lithium-ion-battery_fig2_324929541 [accessed 1 Jul, 2024].

[11] Reniers, J.M., Mulder, G., and Howey, D.A. (2019). Review and performance comparison of mechanical-chemical degradation models for lithium-ion batteries. Journal of The Electrochemical Society, 166(14). https://doi.org/10.1149/2.0281914jes.

[12] Vetter, J. et al. (2005). Ageing mechanisms in lithium-ion batteries. Journal of Power Sources, 147(1-2), 269-281. https://doi.org/10.1016/j.jpowsour.2005.01.006.

[13] Safari, M. et al. (2009). Multimodal physics-based aging model for life prediction of Li-Ion Batteries. Journal of The Electrochemical Society, 156(3), A145. https://doi.org/10.1149/1.3043429.

[14] Sarasketa-Zabala, E. et al. (2015). Cycle ageing analysis of a LiFePO4/graphite cell with dynamic model validations: Towards realistic lifetime predictions. Journal of Power Sources, 275, 573-587. https://doi.org/10.1016/j.jpowsour.2014.10.153.

[15] Attia, P.M. et al. (2019). Electrochemical kinetics of SEI growth on Carbon Black: Part I. Experiments. Journal of The Electrochemical Society, 166(4). https://doi.org/10.1149/2.0231904jes.

[16] Das, S. et al. (2019). Electrochemical kinetics of SEI growth on Carbon Black: Part II. Modeling. Journal of The Electrochemical Society, 166(4). https://doi.org/10.1149/2.0241904jes.

[17] Phung, and Rhee, (2019). A High-Accuracy Model Average Ensemble of Convolutional Neural Networks for Classification of Cloud Image Patches on Small Datasets. Applied Sciences, 9, 4500. https://doi.org/10.3390/app9214500.

[18] Cannizzaro, D., Zafiri, M., Jahier Pagliari, D., Patti, E., Macii, E., Poncino, M., and Acquaviva, A. (2019). A Comparison Analysis of BLE-Based Algorithms for Localization in Industrial Environments. Electronics, 9, 44. https://doi.org/10.3390/electronics9010044.

[19] Shi, L., Du, K., Zhang, C., Ma, H., and Yan, W. (2019). Lung Sound Recognition Algorithm Based on VGGish-BiGRU. IEEE Access, PP, 1-1.

https://doi.org/10.1109/ACCESS.2019.2943492.

[20] Alkhayrat, M., Aljnidi, M., and Aljoumaa, K. (2020). A comparative dimensionality reduction study in telecom customer segmentation using deep learning and PCA. Journal of Big Data, 7, 9. https://doi.org/10.1186/s40537-020-0286-0.

[21] LeCun, Y., Bengio, Y., and Hinton, G. (2015). Deep learning. Nature, 521(7553), 436-444. https://doi.org/10.1038/nature14539.

[22] Girijaprasanna, T., and Dhanamjayulu, C. (2022). A Review on Different State of Battery Charge Estimation Techniques and Management Systems for EV Applications. Electronics, 11(11), 1795. https://www.mdpi.com/2079-9292/11/11/1795.

[23] Lyu, Z., Gao, R., and Li, X. (2021). A partial charging curve-based data-fusion-model method for capacity estimation of Li-Ion battery. Journal of Power Sources, 483, 229131. https://doi.org/10.1016/j.jpowsour.2020.229131.

[24] Richardson, R., et al. (2017). Gaussian process regression for forecasting battery state of health. Journal of Power Sources, 357, 209-219. https://doi.org/10.1016/j.jpowsour.2017.05.004.

[25] Zhao, F., Li, Y., Wang, X., Bai, L., and Liu, T. (2020). Lithium-Ion Batteries State of Charge Prediction of Electric Vehicles Using RNNs-CNNs Neural Networks. IEEE Access, 8, 98168-98180. https://doi.org/10.1109/ACCESS.2020.2995839.

[26] Chen, J., Zhang, Y., Wu, J., Cheng, W., and Zhu, Q. (2023). SOC estimation for lithium-ion battery using the LSTM-RNN with extended input and constrained output. Energy, 262, 125375. https://doi.org/10.1016/j.energy.2022.125375.

[27] Xiang, Y., Fan, W., Zhu, J., Wei, X., and Dai, H. (2024). Semi-supervised deep learning for lithium-ion battery state-of-health estimation using dynamic discharge profiles. Cell Reports Physical Science, 5(1), 101763. https://doi.org/10.1016/j.xcrp.2023.101763.

[28] European Commission, Directorate-General for Research and Innovation, European Group on Ethics in Science and New Technologies, (2018) Statement on artificial intelligence, robotics and 'autonomous' systems : Brussels, 9 March 2018. Publications Office. https://data.europa.eu/doi/10.2777/531856.

8

Appendix

Dataset processing and visualization: Onedrivelink, Megalink
The dataset and code can be accessed through the provided link. This includes a pre-processed file saved as a pickle file for the TUM dataset aswell.

DEPARTMENT OF ELECTRICAL ENGINEERING
CHALMERS UNIVERSITY OF TECHNOLOGY
Gothenburg, Sweden
www.chalmers.se

CHALMERS
UNIVERSITY OF TECHNOLOGY